Eur. Phys. J. C 50, 1–20 (2007)
DOI 10.1140/epjc/s10052-006-0206-2

THE EUROPEAN PHYSICAL JOURNAL C

Regular Article – Experimental Physics

# Diffractive open charm production in deep-inelastic scattering and photoproduction at HERA

The H1 Collaboration

A. Aktas[11], V. Andreev[26], T. Anthonis[4,5], B. Antunovic[27], S. Aplin[11], A. Asmone[34], A. Astvatsatourov[4,5], A. Babaev[25,†], S. Backovic[31], A. Baghdasaryan[39], P. Baranov[26], E. Barrelet[30], W. Bartel[11], S. Baudrand[28], M. Beckingham[11], K. Begzsuren[36], O. Behnke[14,a], O. Behrendt[8], A. Belousov[26], N. Berger[41], J.C. Bizot[28], M.-O. Boenig[8], V. Boudry[29], I. Bozovic-Jelisavcic[2], J. Bracinik[27], G. Brandt[14], M. Brinkmann[11], V. Brisson[28], D. Bruncko[16], F.W. Büsser[12], A. Bunyatyan[13,39], G. Buschhorn[27], L. Bystritskaya[25], A.J. Campbell[11], K.B. Cantun Avila[23], F. Cassol-Brunner[22], K. Cerny[33], V. Cerny[16,48], V. Chekelian[27], J.G. Contreras[23], J.A. Coughlan[6], B.E. Cox[21], G. Cozzika[10], J. Cvach[32], J.B. Dainton[18], K. Daum[38,44], Y. de Boer[25], B. Delcourt[28], M. Del Degan[41], A. De Roeck[11,46], E.A. De Wolf[4,5], C. Diaconu[22], V. Dodonov[13], A. Dubak[31,47], G. Eckerlin[11], V. Efremenko[25], S. Egli[37], R. Eichler[37], F. Eisele[14], A. Eliseev[26], E. Elsen[11], S. Essenov[25], A. Falkewicz[7], P.J.W. Faulkner[3], L. Favart[4,5], A. Fedotov[25], R. Felst[11], J. Feltesse[10,49], J. Ferencei[16], L. Finke[12], M. Fleischer[11], G. Flucke[12], A. Fomenko[26], G. Franke[11], T. Frisson[29], E. Gabathuler[18], E. Garutti[11], J. Gayler[11], S. Ghazaryan[39], S. Ginzburgskaya[25], A. Glazov[11], I. Glushkov[40], L. Goerlich[7], M. Goettlich[11], N. Gogitidze[26], S. Gorbounov[40], M. Gouzevitch[29], C. Grab[41], T. Greenshaw[18], M. Gregori[19], B.R. Grell[11], G. Grindhammer[27], C. Gwilliam[21], S. Habib[12,b], D. Haidt[11], M. Hansson[20], G. Heinzelmann[12], C. Helebrant[11], R.C.W. Henderson[17], H. Henschel[40], G. Herrera[24], M. Hildebrandt[37], K.H. Hiller[40], D. Hoffmann[22], R. Horisberger[37], A. Hovhannisyan[39], T. Hreus[4,5,45], S. Hussain[19], M. Ibbotson[21], M. Jacquet[28], X. Janssen[4,5], V. Jemanov[12], L. Jönsson[20], D.P. Johnson[4,5], A.W. Jung[15], H. Jung[11], M. Kapichine[9], J. Katzy[11], I.R. Kenyon[3], C. Kiesling[27], M. Klein[40], C. Kleinwort[11], T. Klimkovich[11], T. Kluge[11], G. Knies[11], A. Knutsson[20], V. Korbel[11], P. Kostka[40], M. Kraemer[11], K. Krastev[11], J. Kretzschmar[40], A. Kropivnitskaya[25], K. Krüger[15], M.P.J. Landon[19], W. Lange[40], G. Laštovička-Medin[31], P. Laycock[18], A. Lebedev[26], G. Leibenguth[41], V. Lendermann[15], S. Levonian[11], L. Lindfeld[42], K. Lipka[40], A. Liptaj[27], B. List[12], J. List[11], N. Loktionova[26], R. Lopez-Fernandez[24], V. Lubimov[25], A.-I. Lucaci-Timoce[11], H. Lueders[12], L. Lytkin[13], A. Makankine[9], E. Malinovski[26], P. Marage[4,5], R. Marshall[21], L. Marti[11], M. Martisikova[11], H.-U. Martyn[1], S.J. Maxfield[18], A. Mehta[18], K. Meier[15], A.B. Meyer[11], H. Meyer[38], J. Meyer[11], V. Michels[11], S. Mikocki[7], I. Milcewicz-Mika[7], D. Mladenov[35], A. Mohamed[18], F. Moreau[29], A. Morozov[9], J.V. Morris[6], M.U. Mozer[14], K. Müller[42], P. Murín[16,45], K. Nankov[35], B. Naroska[12], T. Naumann[40], P.R. Newman[3], C. Niebuhr[11], A. Nikiforov[27], G. Nowak[7], K. Nowak[42], M. Nozicka[33], R. Oganezov[39], B. Olivier[27], J.E. Olsson[11], S. Osman[20], D. Ozerov[25], V. Palichik[9], I. Panagoulias[11,43,c], M. Pandurovic[2], T. Papadopoulou[11,43,c], C. Pascaud[28], G.D. Patel[18], H. Peng[11], E. Perez[10], D. Perez-Astudillo[23], A. Perieanu[11], A. Petrukhin[25], I. Picuric[31], S. Piec[40], D. Pitzl[11], R. Plačakytė[27], B. Povh[13], P. Prideaux[18], A.J. Rahmat[18], N. Raicevic[31], P. Reimer[32], A. Rimmer[18], C. Risler[11], E. Rizvi[19], P. Robmann[42], B. Roland[4,5], R. Roosen[4,5], A. Rostovtsev[25], Z. Rurikova[11], S. Rusakov[26], F. Salvaire[11], D.P.C. Sankey[6], M. Sauter[41], E. Sauvan[22], S. Schmidt[11], S. Schmitt[11], C. Schmitz[42], L. Schoeffel[10], A. Schöning[41], H.-C. Schultz-Coulon[15], F. Sefkow[11], R.N. Shaw-West[3], I. Sheviakov[26], L.N. Shtarkov[26], T. Sloan[17], I. Smiljanic[2], P. Smirnov[26], Y. Soloviev[26], D. South[11], V. Spaskov[9], A. Specka[29], M. Steder[11], B. Stella[34], J. Stiewe[15], A. Stoilov[35], U. Straumann[42], D. Sunar[4,5], T. Sykora[4,5], V. Tchoulakov[9], G. Thompson[19], P.D. Thompson[3], T. Toll[11], F. Tomasz[16], D. Traynor[19], T.N. Trinh[22], P. Truöl[42], I. Tsakov[35], G. Tsipolitis[11,43], I. Tsurin[11], J. Turnau[7], E. Tzamariudaki[27], K. Urban[15], M. Urban[42], A. Usik[26], D. Utkin[25], A. Valkárová[33], C. Vallée[22], P. Van Mechelen[4,5], A. Vargas Trevino[8], Y. Vazdik[26], S. Vinokurova[11], V. Volchinski[39], K. Wacker[8], G. Weber[12], R. Weber[41], D. Wegener[8], C. Werner[14], M. Wessels[11], C. Wissing[11], R. Wolf[14], E. Wünsch[11], S. Xella[42], W. Yan[11], V. Yeganov[39], J. Žáček[33], J. Zálešák[32], Z. Zhang[28], A. Zhelezov[25], A. Zhokin[25], Y.C. Zhu[11], J. Zimmermann[27], T. Zimmermann[41], H. Zohrabyan[39], F. Zomer[28]

[1] I. Physikalisches Institut der RWTH, Aachen, Germany[d]
[2] Vinca Institute of Nuclear Sciences, Belgrade, Serbia
[3] School of Physics and Astronomy, University of Birmingham, Birmingham, UK[e]
[4] Inter-University Institute for High Energies ULB-VUB, Brussels, Belgium[f]
[5] Universiteit Antwerpen, Antwerpen, Belgium[f]
[6] Rutherford Appleton Laboratory, Chilton, Didcot, UK[e]
[7] Institute for Nuclear Physics, Cracow, Poland[g]
[8] Institut für Physik, Universität Dortmund, Dortmund, Germany[d]

[9] Joint Institute for Nuclear Research, Dubna, Russia
[10] CEA, DSM/DAPNIA, CE-Saclay, Gif-sur-Yvette, France
[11] DESY, Hamburg, Germany
[12] Institut für Experimentalphysik, Universität Hamburg, Hamburg, Germany[d]
[13] Max-Planck-Institut für Kernphysik, Heidelberg, Germany
[14] Physikalisches Institut, Universität Heidelberg, Heidelberg, Germany[d]
[15] Kirchhoff-Institut für Physik, Universität Heidelberg, Heidelberg, Germany[d]
[16] Institute of Experimental Physics, Slovak Academy of Sciences, Košice, Slovak Republic[h]
[17] Department of Physics, University of Lancaster, Lancaster, UK[e]
[18] Department of Physics, University of Liverpool, Liverpool, UK[e]
[19] Queen Mary and Westfield College, London, UK[e]
[20] Physics Department, University of Lund, Lund, Sweden[i]
[21] Physics Department, University of Manchester, Manchester, UK[e]
[22] CPPM, CNRS/IN2P3, Univ. Mediterranee, Marseille, France
[23] Departamento de Fisica Aplicada, CINVESTAV, Mérida, Yucatán, México[j]
[24] Departamento de Fisica, CINVESTAV, México[j]
[25] Institute for Theoretical and Experimental Physics, Moscow, Russia[k]
[26] Lebedev Physical Institute, Moscow, Russia[l]
[27] Max-Planck-Institut für Physik, München, Germany
[28] LAL, Université de Paris-Sud 11, IN2P3-CNRS, Orsay, France
[29] LLR, Ecole Polytechnique, IN2P3-CNRS, Palaiseau, France
[30] LPNHE, Universités Paris VI and VII, IN2P3-CNRS, Paris, France
[31] Faculty of Science, University of Montenegro, Podgorica, Montenegro[l]
[32] Institute of Physics, Academy of Sciences of the Czech Republic, Praha, Czech Republic[m]
[33] Faculty of Mathematics and Physics, Charles University, Praha, Czech Republic[m]
[34] Dipartimento di Fisica Università di Roma Tre and INFN Roma 3, Roma, Italy
[35] Institute for Nuclear Research and Nuclear Energy, Sofia, Bulgaria[l]
[36] Institute of Physics and Technology of the Mongolian Academy of Sciences, Ulaanbaatar, Mongolia
[37] Paul Scherrer Institut, Villigen, Switzerland
[38] Fachbereich C, Universität Wuppertal, Wuppertal, Germany
[39] Yerevan Physics Institute, Yerevan, Armenia
[40] DESY, Zeuthen, Germany
[41] Institut für Teilchenphysik, ETH, Zürich, Switzerland[n]
[42] Physik-Institut der Universität Zürich, Zürich, Switzerland[n]
[43] Also at Physics Department, National Technical University, Zografou Campus, 15773 Athens, Greece
[44] Also at Rechenzentrum, Universität Wuppertal, Wuppertal, Germany
[45] Also at University of P.J. Šafárik, Košice, Slovak Republic
[46] Also at CERN, Geneva, Switzerland
[47] Also at Max-Planck-Institut für Physik, München, Germany
[48] Also at Comenius University, Bratislava, Slovak Republic
[49] Also at DESY and University Hamburg, Germany, Helmholtz Humboldt Research Award

[†] deceased

Received: 25 October 2006 / Revised version: 24 November 2006 /
Published online: 8 February 2007 – 

**Abstract.** Measurements are presented of diffractive open charm production at HERA. The event topology is given by $ep \to eXY$ where the system $X$ contains at least one charmed hadron and is well separated by a large rapidity gap from a leading low-mass proton remnant system $Y$. Two analysis techniques are used for the cross section measurements. In the first, the charm quark is tagged by the reconstruction of a $D^{*\pm}(2010)$ meson. This technique is used in deep-inelastic scattering (DIS) and photoproduction ($\gamma p$). In the second, a method based on the displacement of tracks from the primary vertex is used to measure the open charm contribution to the inclusive diffractive cross section in DIS. The measurements are compared with next-to-leading order QCD predictions based on diffractive parton density functions previously obtained from a QCD analysis of the inclusive diffractive cross section at H1. A good agreement is observed in the full kinematic regime, which supports the validity of QCD factorization for open charm production in diffractive DIS and $\gamma p$.

[a] e-mail: obehnke@mail.desy.de

[b] Supported by a scholarship of the World Laboratory Björn
Wiik Research Project

## 1 Introduction

Diffractive processes in positron–proton ($ep$) collisions are those where the hadronic final state is separated by a large gap in rapidity, without hadrons, into two systems $X$ and $Y$, where the system $Y$ may consist only of a proton or low mass system. The system $X$ is known as the photon dissociative system. The diffractive event signature is understood to arise from a color singlet exchange between the two systems $X$ and $Y$.

In quantum chromodynamics (QCD), the theory of strong interactions, the hard scattering collinear factorization theorem [1, 2] predicts that the cross section for diffractive deep-inelastic $ep$ scattering (DIS) factorizes into a set of universal diffractive parton density functions (DPDFs) of the proton and process-dependent hard scattering coefficients. Next-to-leading order (NLO) DPDFs have been determined by QCD fits to the measured cross sections of inclusive diffractive scattering at HERA [3, 4] within the factorizable pomeron model [5–7] and using the DGLAP evolution equations [8–11]. The DPDFs have been found to be dominated by gluons, which carry $\approx 70\%$ of the momentum of the diffractive exchange.

If QCD factorization is fulfilled, NLO QCD calculations based on the diffractive parton density functions of [3, 4], should be able to predict the production rates of more exclusive diffractive processes like dijet and open charm production in shape and normalization. For diffractive dijet production this has been tested in photoproduction ($\gamma p$) and in DIS [12–14].

In the collinear factorization approach diffractive open charm production at HERA is expected mainly to proceed via boson gluon fusion (BGF) as depicted in Fig. 1a. Thus it is directly sensitive to the gluon content of the diffractive exchange, which is only determined indirectly and for low momentum fractions $z_{I\!P}$ of the gluon in inclusive diffractive scattering via scaling violations [4]. In the BGF process a charm quark anti-quark pair ($c\bar{c}$) is produced where one quark couples to the photon with virtuality $Q^2$ and the other to a gluon that emerges from the diffractive exchange.

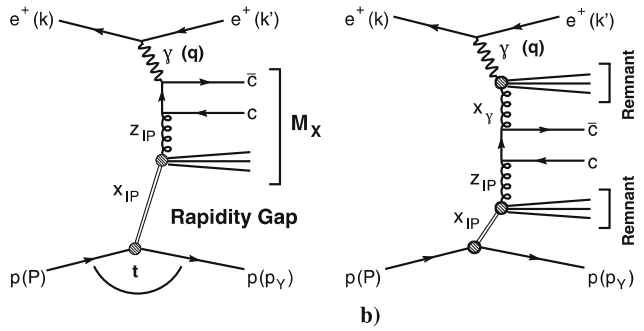


**Fig. 1.** The main processes of diffractive open charm production at HERA in the collinear factorization approach. **a** shows the direct process where the photon enters the hard scatter itself; **b** shows the resolved photon process where only a reduced fraction $x_\gamma$ of the photon's momentum takes part in the hard scatter

In Fig. 1a the "direct photon" process is shown, where the photon itself enters the hard scatter, which is expected to be dominant for $c\bar{c}$-production in DIS and photoproduction. In photoproduction, however, the quasi real photon may also evolve an hadronic structure, as indicated in Fig. 1b, before it enters the hard scatter. In this case only a fraction $x_\gamma < 1$ of the photon's momentum takes part in the scattering process; the rest forming a remnant. In these "resolved photon" processes initial state interactions may take place between the photon- and the proton-remnant systems, destroying the rapidity gap signature and thus the diffractive nature of the process. A breakdown of QCD factorization has been observed for diffractive dijet production in $p\bar{p}$ collisions at the Tevatron [15], where the prediction overestimates the observed rate by approximately one order of magnitude. Diffractive open charm production is suitable for testing a potential suppression of diffractive processes in photoproduction.

In an alternative theoretical approach DPDFs are not introduced and diffractive scattering is explicitly modeled by the perturbative exchange of a colorless gluon state (two gluons or a gluon ladder). Formulated in the proton rest frame the "two-gluon" state of the proton can couple directly to the $c\bar{c}$ pair ($\gamma^* p \to c\bar{c}p$) or to a $c\bar{c}g$ color dipole fluctuation of the photon ($\gamma^* p \to c\bar{c}gp$) [16–20]. The gluon density of the proton is usually determined from fits to the inclusive DIS cross section in the $k_t$-factorization [21] scheme. A model combining the perturbative two-gluon approach with the collinear factorization scheme, which has also been used to fit the HERA diffractive DIS cross sections, is given in [22–24].

Two methods to identify charm production are presented in this paper. In the first method the charm quark is tagged by the reconstruction of $D^*$ mesons. The measurement is performed in DIS and extended to $\gamma p$, where

[c] This project is co-funded by the European Social Fund (75%) and National Resources (25%) – (EPEAEK II) – PYTHAGORAS II

[d] Supported by the Bundesministerium für Bildung und Forschung, FRG, under contract numbers 05 H1 1GUA/1, 05 H1 1PAA/1, 05 H1 1PAB/9, 05 H1 1PEA/6, 05 H1 1VHA/7 and 05 H1 1VHB/5

[e] Supported by the UK Particle Physics and Astronomy Research Council, and formerly by the UK Science and Engineering Research Council

[f] Supported by FNRS-FWO-Vlaanderen, IISN-IIKW and IWT and by Interuniversity Attraction Poles Programme, Belgian Science Policy

[g] Partially supported by the Polish State Committee for Scientific Research, SPUB/DESY/P003/DZ 118/2003/2005

[h] Supported by VEGA SR grant no. 2/4067/24

[i] Supported by the Swedish Natural Science Research Council

[j] Supported by CONACYT, México, grant 400073-F

[k] Partially Supported by Russian Foundation for Basic Research, grants 03-02-17291 and 04-02-16445

[l] Supported by the Deutsche Forschungsgemeinschaft

[m] Supported by the Ministry of Education of the Czech Republic under the projects LC527 and INGO-1P05LA259

[n] Supported by the Swiss National Science Foundation

it represents the first cross section measurement of diffractive open charm production at HERA. In DIS it supercedes a former analysis of H1 [25] with increased statistics and with reduced systematic uncertainties. A similar measurement in DIS was performed by the ZEUS collaboration [26]. The results are presented in the form of integrated and differential $D^*$ cross sections and in DIS are extrapolated into the unmeasured phase space of the $D^*$ meson using NLO QCD calculations in order to determine the open charm contribution to the diffractive cross section. The second method, which was used to measure the total inclusive charm and beauty cross sections in DIS [27, 28], is used here for the first time in diffractive DIS. In this method, referred to in the following as the 'displaced track analysis', the charm quark is identified by the reconstruction of tracks, which are displaced from the interaction vertex, that arise due to long lived charmed hadrons. This method is used in a kinematic region with high acceptance for the decay products of charmed hadrons within the silicon vertex detector of H1, which is used in the reconstruction of these tracks. With this method it is thus possible to measure the total open charm contribution to the diffractive cross section with small extrapolations from QCD calculations.

In Sect. 2 the kinematic variables used throughout the paper are introduced. A short discussion of the H1 detector and the event selection are given in Sects. 3 and 4, followed by a description of the event simulation in Sect. 5 and the cross section determination with the two independent methods in Sect. 6. The NLO QCD calculations and the comparison of the measured cross sections with the NLO QCD calculations are discussed in Sects. 7 and 8.

## 2 Kinematics of diffractive $ep$ scattering

Due to the diffractive nature of the process the photon (with four-momentum $q$) and the proton (with four-momentum $P$) dissociate into two distinct hadronic systems $X$ and $Y$ (with four-momenta $p_X$ and $p_Y$, respectively), which are separated by a large gap in rapidity between the final state hadrons. The kinematics of the inclusive $ep$ scattering are fully determined by the negative squared four momentum transfer of the exchanged photon $Q^2$, the squared center of mass energy of the $ep$ scattering process $s$ and the inelasticity $y$. In addition, the following variables are defined to characterize the diffractive nature of the process

$$M_Y^2 = p_Y^2\,, \qquad t = (P - p_Y)^2,$$
$$x_{I\!P} = \frac{q\cdot(P-p_Y)}{q\cdot P}\,, \qquad \beta = \frac{Q^2}{2q\cdot(P-p_Y)}\,, \tag{1}$$

where $M_Y$ and $t$ denote the invariant mass of the system $Y$ and the squared four-momentum transferred at the proton vertex, respectively. The variable $x_{I\!P}$ can be interpreted as the longitudinal momentum fraction of the diffractive exchange with respect to the proton. The variable $\beta$ (which is only defined in DIS) corresponds to the Bjorken $x$ variable from inclusive scattering taken with respect to the diffractive exchange. The quantities $t$ and $M_Y$ are constrained to be small by the experimental selection and are integrated over implicitly. For the $D^*$ analyses the observable $z_{I\!P}^{\rm obs}$ is introduced as

$$z_{I\!P}^{\rm obs} = \frac{Q^2 + \hat{s}^{\rm obs}}{x_{I\!P}\cdot y\cdot s}\,, \tag{2}$$

where $\hat{s}^{\rm obs}$ is a hadron level estimate of the invariant mass of the $c\bar{c}$ pair emerging from the hard scattering process. It is reconstructed from the scattered positron and the kinematics of the reconstructed $D^*$ meson including an approximate correction of the momentum of the $D^*$ meson to the momentum of the charm quark [25]. In BGF processes $z_{I\!P}^{\rm obs}$ is a direct estimator for the longitudinal momentum fraction $z_{I\!P}$ of the gluon that enters the scattering process with respect to the momentum of the diffractive exchange.

## 3 The H1 detector

A detailed description of the H1 detector can be found in [29, 30]. Only the components most relevant for this analysis are briefly discussed here. The coordinate system is centered at the nominal $ep$ interaction point with the $z$-axis pointing along the beam direction of the outgoing proton, also referred to as the 'forward' direction in the following. Charged particles emerging from the interaction region are measured by the central tracking detector (CTD), which covers a range of $-1.74 < \eta < 1.74$ in pseudorapidity[1]. The CTD comprises two large cylindrical central jet drift chambers (CJCs) and two $z$ chambers situated concentrically around the beam-line within a solenoidal magnetic field of 1.15 T. It also provides triggering information based on track segments measured in the $r$-$\phi$ plane of the CJCs, and on the $z$ position of the event vertex obtained from the double layers of two multiwire proportional chambers (MWPCs). The CTD tracks are linked to hits in the central silicon tracker (CST) [31] to provide precise spatial track reconstruction. The CST consists of two layers of double-sided silicon strip detectors surrounding the beam pipe, with a coverage of $-1.3 < \eta < 1.3$ in pseudorapidity for tracks passing through both layers.

The tracking detectors are surrounded by a liquid argon calorimeter (LAr) in the forward and central region ($-1.5 < \eta < 3.4$) and by a lead-scintillating fiber calorimeter (SpaCal) with electromagnetic and hadronic sections in the backward region [32] ($-4 < \eta < -1.4$). These calorimeters provide energy and angular reconstruction for final state particles from the hadronic system. DIS events are identified by the energy deposits of the scattered positron in the SpaCal calorimeter. Photoproduction events are selected with a crystal Čerenkov calorimeter located close to the beam pipe at $z = -33.4\,\mathrm{m}$ in the positron direction

[1] The pseudorapidity $\eta$ of an object detected with polar angle $\theta$ is defined as $\eta = -\ln\tan(\theta/2)$.

(electron tagger), which measures the energy deposits of positrons scattered by angles of less than 5 mrad. Another Čerenkov calorimeter located at $z = -103$ m is used to determine the $ep$ luminosity by detecting the radiated photon emitted in the Bethe–Heitler process ($ep \to ep\gamma$).

For the rapidity gap selection a set of detectors close to the beam pipe in the forward direction is used. The forward muon detector (FMD) is located at $z = 6.5$ m and covers a pseudorapidity range of $1.9 < \eta < 3.7$. It may also detect particles produced at larger $\eta$ due to secondary scattering within the beam pipe. A PLUG hadronic sampling calorimeter allows energy measurements in the range of $3.5 < \eta < 5.5$. Finally, particles in the region of $6.0 \lesssim \eta \lesssim 7.5$ can be detected by the proton remnant tagger (PRT), a set of scintillation counters surrounding the beam pipe at $z = 26$ m.

## 4 Event selection

The data presented in this analysis were collected over the years 1999 and 2000 and correspond to an integrated luminosity of $\mathcal{L} = 47.0\,\mathrm{pb}^{-1}$ for the $D^*$ analyses and $48.3\,\mathrm{pb}^{-1}$ for the displaced track analysis. At this time HERA was operated with positrons of energy 27.6 GeV and protons of energy 920 GeV so that the center of mass energy of the $ep$ collision is $\sqrt{s} = 318$ GeV.

DIS events are triggered by an electromagnetic energy cluster in the SpaCal calorimeter. In the $D^*$ analyses the trigger further requires a charged track signal in the CTD and a reconstructed event vertex, while a looser track requirement of hits in the MWPCs is used in the trigger for the displaced track analysis. In the offline analyses the scattered positron is selected as an electromagnetic SpaCal cluster with energy $E'_e > 8$ GeV. Photoproduction events are suppressed by requiring $\sum_i (E_i - p_{z,i}) > 35$ GeV. Here, $E_i$ and $p_{z,i}$ denote the energy and longitudinal momentum components of a particle and the sum is over all final state particles including the scattered positron and the hadronic final state (HFS). The HFS particles are reconstructed using a combination of tracks and calorimeter deposits in an energy flow algorithm that avoids double counting. The $z$ position of the interaction vertex is required to lie within $\pm 35$ cm ($\pm 20$ cm) of the center of the CTD for the $D^*$ (displaced track) analyses, where the reduced range in the displaced track analysis is chosen in order to match the smaller acceptance of the CST. The kinematic variables of the DIS scattering process $Q^2$ and $y$ are reconstructed using a method which uses the angle of the hadronic final state in addition to the energy and the polar angle of the scattered positron [4]. The accepted kinematic range in DIS is restricted to $2 < Q^2 < 100\,\mathrm{GeV}^2$ and $0.05 < y < 0.7$ for the $D^*$ analysis and to $15 < Q^2 < 100\,\mathrm{GeV}^2$ and $0.07 < y < 0.7$ for the displaced track analysis, where the reduced kinematic range in the displaced track analysis is chosen such that the direction of the quark struck by the photon mostly lies within the angular acceptance of the CST and that the HFS has a significant transverse momentum.

Photoproduction events are selected by a trigger that requires a scattered positron to be measured in the electron tagger, a charged track signal in the CTD and a reconstructed event vertex. The events have passed an additional online software filter that selects events with candidates for charmed hadron decays by calculating the invariant mass of track combinations. The inelasticity $y$ is reconstructed from the energy of the scattered positron and is restricted to the range $0.3 < y < 0.65$. The photon virtuality is experimentally restricted to $Q^2 < 0.01\,\mathrm{GeV}^2$.

In all analyses presented in this paper diffractive events are selected by the absence of hadronic activity above noise thresholds in the most forward part of the LAr calorimeter ($\eta > 3.2$) and in the forward detectors. This selection ensures that the gap between the systems $X$ and $Y$ spans more than 4 units between $\eta = 3.2$ and 7.5 in pseudorapidity. As $M_Y$ is not directly measurable by this method the data are corrected to a visible range of $M_Y < 1.6$ GeV and $|t| < 1\,\mathrm{GeV}^2$, consistent with former measurements [4, 12–14, 25], with the help of Monte Carlo simulations. The variable $x_{I\!P}$ is calculated from

$$x_{I\!P} = \frac{Q^2 + M_X^2}{s \cdot y}\,, \quad M_X^2 = \sum_i \left(E_i^2 - p_{i,x}^2 - p_{i,y}^2 - p_{i,z}^2\right), \tag{3}$$

where the sum for the calculation of $M_X$ runs over all HFS objects in the system $X$. Each of the presented analyses is restricted to $x_{I\!P} < 0.04$, which suppresses contributions from non-diffractive scattering and secondary reggeon exchanges. The displaced track analysis is further restricted to $M_X > 6$ GeV.

## 5 Event simulation and acceptance correction

The data are corrected for trigger efficiencies, detector acceptances, efficiencies, and migration effects due to the finite resolution of the H1 detector using a Monte Carlo simulation. All the generated events are passed through a detailed simulation of the detector response based on the GEANT simulation program [33] and reconstructed using the same reconstruction software as used for the data. For the event simulation residual noise contributions in the LAr calorimeter and the forward detectors are taken into account.

Events are generated using the RAPGAP event generator [34], which simulates the process $e^+p \to e^+Xp$ with $x_{I\!P} < 0.15$, assuming proton vertex factorization. Both pomeron and reggeon sub-leading exchanges are included. The $t$ dependence is of the form $\mathrm{d}\sigma/\mathrm{d}t \propto \mathrm{e}^{B_{\mathrm{EL}}t}$ with a slope parameter $B_{\mathrm{EL}} = 6\,\mathrm{GeV}^{-2}$. For the simulation of diffractive events containing charm quarks RAPGAP implements the BGF process in leading order (LO) of pQCD. For the $D^*$ analyses LO DPDFs are taken from a former analysis of H1 [3]. For the displaced track analysis the DPDFs are taken from [4]. To simulate higher order effects of QCD, parton showers are included in the calculations. Fragmentation is performed according to the Lund

string model [35]. In DIS RAPGAP is interfaced to the QED simulation program HERACLES [36] to evaluate the radiative effects of QED. For diffractive photoproduction the contributing diagrams of charm excitation and other resolved photon processes are included in the event generation, using the LO parton distribution functions for the resolved photon obtained in [37, 38]. In the excitation processes the charm quark is treated as a massless parton in the resolved photon, whereas in all other processes the charm mass is taken into account in the calculations. The resolved processes are found to contribute less then 10% of the charm signal and to be mainly concentrated at large values of $x_{I\!P}$ and small values of $p_{\rm t}(D^*)$ and $z_{I\!P}^{\rm obs}$.

Due to the limited detector acceptance in the forward region of H1 it is not possible to efficiently detect a break-up of the proton into a low mass resonant state $Y$. To keep the uncertainties arising from such proton dissociation processes small the measurement is integrated over the region $M_Y < 1.6\,\text{GeV}$ and $|t| < 1\,\text{GeV}^2$. Diffractive proton dissociative events in the region $M_Y < 5\,\text{GeV}$ are simulated using RAPGAP with a cross section dependence of the form $\mathrm{e}^{B_{\rm PD}t}$ with $B_{\rm PD} = 1.6\,\text{GeV}^{-2}$ and an approximate $M_Y$ dependence of the form $\mathrm{d}\sigma/\mathrm{d}M_Y^2 \propto 1/M_Y^2$ [39]. The correction factor $\delta^{p\rm dis}$ for migrations across the measurement boundary is evaluated in the simulation for each kinematic bin. In the simulations the ratio of proton elastic to proton dissociative interactions is taken to be 1 : 1, which is in accordance with the inclusive measurements of [4, 40]. The value of $\delta^{p\rm dis}$ is found to be in the range 0.88–0.97.

Non-diffractive events with $M_Y > 5\,\text{GeV}$ or $x_{I\!P} > 0.15$ are simulated by RAPGAP in DIS and by the event generator PYTHIA [41] in photoproduction. The non-diffractive background contribution in the final event selections is estimated to be less than 3% for all data samples.

## 6 Open charm selection

Charm quarks are selected by two independent methods. In the first method they are selected by the full reconstruction of $D^*$ mesons. This provides a clear signature, which enables the tagging of charm quarks in DIS and photoproduction. In the second method the more general character of the long lifetime of charmed hadrons is used, by reconstructing the displacement of tracks from the primary vertex in the CST of H1, similarly to inclusive charm production measurements in [27, 28]. This provides the advantage of a high acceptance for charm quarks and small correction factors for extrapolations to the full phase space. It is therefore especially suited for a measurement of the total diffractive charm cross section.

### 6.1 Diffractive $D^*$ analyses

In the $D^*$ analyses $D^{*\pm}$ mesons are fully reconstructed using the decay channel

$$D^{*+} \to D^0\pi^+_{\rm slow} \to (K^-\pi^+)\pi^+_{\rm slow}\,(+\text{C.C.})\,, \qquad (4)$$

which has a branching ratio of 2.57% [42]. The decay products are detected in the CTD. To ensure good detection efficiency and to reduce combinatorial background, the tracks are required to lie within an angular range of $20^\circ < \theta < 160^\circ$ and to have a transverse momentum $p_{\rm t}$ relative to the beam axis of at least 120 MeV for the $\pi_{\rm slow}$, 300 MeV for the other pion and 500 MeV for the $K$ candidate. The invariant mass of the $K\pi$ combination has to be consistent with the $D^0$ mass within $\pm 80$ MeV. The transverse momentum and pseudorapidity of the reconstructed $D^*$ meson candidate are restricted to $p_{\rm t}(D^*) > 2$ GeV and $|\eta(D^*)| < 1.5$. The distributions of the mass difference $\Delta M = M(K^\mp\pi^\pm\pi^\pm_{\rm slow}) - M(K^\mp\pi^\pm)$ for all track combinations which fulfill the above requirements for all selected events in DIS and photoproduction are shown in Fig. 2. The number of $D^{*\pm}$ mesons is determined by fitting these distributions with a Gaussian function for the signal plus a background parameterization given by $N(\Delta M - m_\pi)^{u_e}(1 - u_s(\Delta M)^2)$, where $m_\pi$ denotes the mass of the charged pion and $N$, $u_e$ and $u_s$ are free parameters. The position and the width of the Gaussian function are fixed

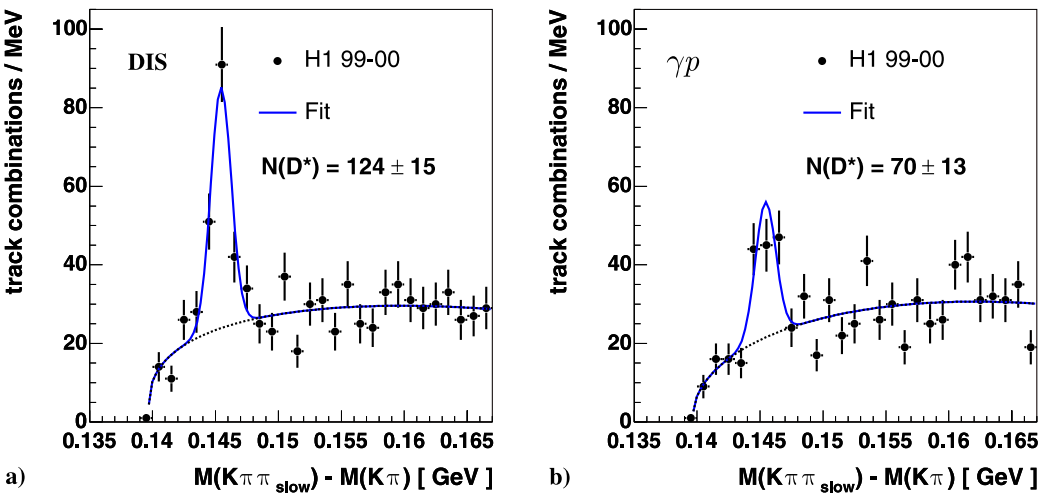


**Fig. 2.** The $\Delta M$ distribution for each track combination that passes the selections described in Sects. 4 and 6.1 for **a** DIS and **b** photoproduction. The parameterization used to obtain the number of reconstructed $D^*$ mesons shown in the plot is described in the text

**Table 1.** Measured cross sections and NLO QCD predictions for diffractive $D^*$ meson production in the visible ranges of DIS and photoproduction ($\gamma p$). The uncertainty on the NLO QCD predictions is given by the variation of the mass, the scale and the fragmentation parameters as described in the text

| | H1 99–00 | $N(D^*)$ | Cross section [pb] | | |
|---|---|---|---|---|---|
| | | | Data | H1 2006 DPDF | |
| | | | | Fit A | Fit B |
| DIS | $0.05 < y < 0.7$ | $124 \pm 15$ | $234 \pm 29(\text{stat.}) \pm 34(\text{syst.})$ | $287^{+81}_{-70}$ | $272^{+78}_{-71}$ |
| | $0.3 < y < 0.65$ | $34 \pm 8$ | $55 \pm 16(\text{stat.}) \pm 9(\text{syst.})$ | $86^{+20}_{-18}$ | $84^{+20}_{-18}$ |
| $\gamma p$ | $0.3 < y < 0.65$ | $70 \pm 13$ | $265 \pm 50(\text{stat.}) \pm 41(\text{syst.})$ | $360^{+90}_{-70}$ | $359^{+93}_{-75}$ |

to values taken from higher statistics samples where no diffractive cuts were applied. The resulting numbers of identified $D^{*\pm}$ mesons in DIS and photoproduction are summarized in Table 1.

Differential cross sections are obtained from the fitted number of $D^*$ mesons in each measurement bin. A correction is applied for mass reflections originating from decays of the $D^0$ meson other than that given in (4), which has been estimated to be 3.5% of the $D^*$ signal [43]. A correction factor of $\simeq 0.95$ for the effects of initial and final state QED radiation is applied to the DIS cross sections. The cross sections are bin center corrected using RAPGAP to determine the point in the bin at which the bin-averaged cross section equals the differential cross section.

### 6.2 Displaced track analysis

The production of open charm in diffraction is also investigated using a largely independent method, which has been used in [27] and [28] to measure the total inclusive charm and beauty cross sections in DIS. This method distinguishes events containing heavy quarks from those containing only light quarks by reconstructing the displacement of tracks from the primary vertex in the transverse plane (impact parameter), caused by the long lifetimes of the charm and beauty flavored hadrons, using the precise spatial information from the CST of H1. Due to the low beauty fraction in the diffractive data sample, it is not possible to make a measurement of the beauty cross section and only a measurement of the charm cross section is presented in this paper.

As in [27, 28] the primary event vertex in the $r$–$\phi$ plane is reconstructed from all tracks (with or without hits in the CST) using the information on the position and transverse extent of the beam interaction region. For the analysis, tracks are selected if they have a transverse momentum of more than 0.5 GeV and at least two associated hits in the CST. The impact parameter of a track is defined as the distance of closest approach (DCA) of the track to the primary vertex point in the transverse plane.

In order to determine a signed impact parameter ($\delta$) for a track, the azimuthal angle of the struck quark $\phi_{\text{quark}}$ must be determined for each event. To do this, jets with a minimum $p_{\text{t}}$ of 2.5 GeV, in the angular range $15^\circ < \theta < 155^\circ$, are reconstructed using the invariant $k_{\text{t}}$ algorithm [44, 45] in the laboratory frame using all reconstructed HFS particles. The angle $\phi_{\text{quark}}$ is defined as the $\phi$ of the jet with the highest transverse momentum or, if there is no jet reconstructed in the event, as $180^\circ - \phi_{\text{elec}}$, where $\phi_{\text{elec}}$ is the azimuthal angle of the scattered positron in degrees. Monte Carlo simulations indicate that $\approx 78\%$ of all charm events have at least one reconstructed jet in the kinematic region described above. The direction defined by the primary vertex and $\phi_{\text{quark}}$ in the transverse plane is called the 'quark axis'. If the angle between the quark axis and the line joining the primary vertex to the point of DCA of the track is less than $90^\circ$, $\delta$ is defined as positive, and is defined as negative otherwise. Tracks with azimuthal angle outside $\pm 90^\circ$ of $\phi_{\text{quark}}$ are rejected. The estimated error on $\delta$ is denoted as $\sigma(\delta)$.

To distinguish between the charm and light quark flavors a similar method to that in [28] is used. The quantity $S_1$ ($S_2$) is defined as the significance ($\delta/\sigma(\delta)$) of the track with the highest (second highest) absolute significance that is associated to the quark axis. In the present analysis $S_3$, which is the significance of the track with the third highest absolute significance, is not used due to lower statistics than in [28]. Events where $S_1$ and $S_2$ have opposite signs are excluded from the $S_2$ distribution, but contribute to the $S_1$ distribution. The distributions of $S_1$ and $S_2$ are shown in Fig. 3 for the kinematic region given in Sect. 4. A reasonable description of the data by the simulation is observed. The light quark significance distributions are approximately symmetric around zero, whereas the charm distributions have an excess in the positive bins compared with the negative. It is thus possible to substantially reduce the uncertainty due to the resolution of $\delta$ and the light quark normalization, by subtracting the contents of the negative bins in the significance distributions from the contents of the corresponding positive bins. The subtracted distributions are shown in Fig. 4.

The fractions of charm and light quark flavors in the data are extracted in three $M_X^2$ intervals using a least squares simultaneous fit to the subtracted $S_1$ and $S_2$ distributions (as shown in Fig. 4) and the total number of reconstructed diffractive events before any track selection. The significance distributions of the charm, beauty and

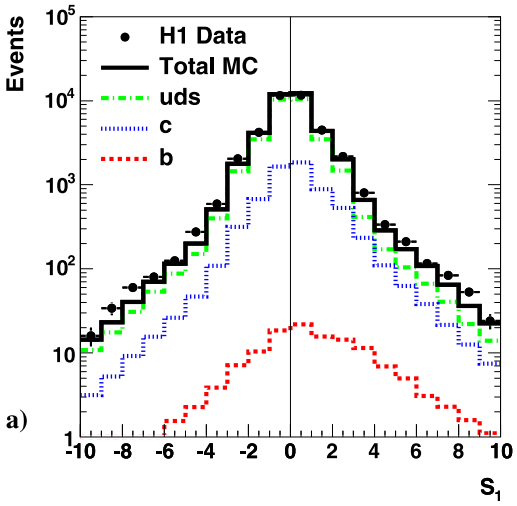


**Fig. 3.** The significance $\delta/\sigma(\delta)$ distribution **a** of the highest absolute significance track ($S_1$) and **b** of the track with the second highest absolute significance ($S_2$). Included in the figure is the expectation from the Monte Carlo simulation program RAPGAP for light, charm and beauty quarks. The contributions from the various quark flavors are shown after applying the scale factors obtained from the fit to the subtracted significance distributions of the data shown in Fig. 4

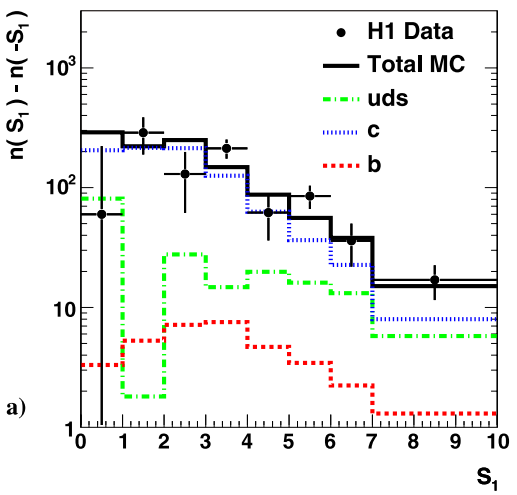


**Fig. 4.** The subtracted significance distributions of **a** $S_1$ and **b** $S_2$. Included in the figure is the result from the fit of the Monte Carlo distributions of the various quark flavors to the data

light flavors, as predicted by the Monte Carlo simulation for the luminosity of the data, are used as templates. In each interval the charm and light quark flavor contributions from the Monte Carlo simulation are scaled by factors $P_c$ and $P_l$, respectively, to give the best fit to the observed subtracted $S_1$, $S_2$ distributions and the total number of events. Since the same event may enter the $S_1$ and the $S_2$ distributions, it was checked using a high statistics Monte Carlo simulation that this has a negligible effect on the results of the fits with the statistics of the present data. Only the statistical errors of the data and the Monte Carlo simulation are taken into account in the fit. The beauty scale factor is fixed to $P_b = 1$, and varied in the evaluation of the systematic uncertainties (see Sect. 6.3). The results of the fit to the complete data sample are shown in Fig. 4. The fit gives a good description of all significance distributions, with a $\chi^2$/n.d.f of 18.1/12. Values of $P_c = 0.77 \pm 0.09$ and $P_l = 0.97 \pm 0.03$ are obtained. It can be seen that the resulting distributions are dominated by charm quark events, the light quarks contributing only a small fraction, mainly due to strange hadrons, for all values of the significance. The beauty contribution forms a small fraction overall, but increases with increasing $M_X^2$. Acceptable $\chi^2$ values are also found for the fits to the samples in the separate $M_X^2$ intervals.

The results of the fit in each $M_X^2$ interval are converted to a measurement of the diffractive differential cross section using:

$$\frac{\mathrm{d}^3\sigma_D^{c\bar{c}}}{\mathrm{d}Q^2\,\mathrm{d}y\,\mathrm{d}M_X^2} = \frac{P_c N_c^{\mathrm{MCgen}} \delta_c^{\mathrm{rad}} \delta^{p\mathrm{dis}} \delta_c^{\mathrm{BCC}}}{\mathcal{L}\cdot \mathrm{BV}}\,, \qquad (5)$$

where $N_c^{\mathrm{MCgen}}$ is the number of generated charm events expected from the Monte Carlo simulation in each bin with volume BV corresponding to the luminosity of the data $\mathcal{L}$. A bin center correction $\delta_c^{\mathrm{BCC}}$ in the range 0.89–1.21 is calculated using the NLO QCD expectation to correct the bin averaged cross section to the cross section at a specified point in $Q^2$, $y$ and $M_X^2$. A correction factor of $\delta_c^{\mathrm{rad}} \simeq 0.93$ for initial and final state QED radiation is applied. The correction factor for proton dissociation $\delta^{p\mathrm{dis}}$ is described in Sect. 5.

Measurements of the ratio of the diffractive charm cross section to the total diffractive cross section are made where

the total diffractive cross section is determined using

$$\frac{\mathrm{d}^3\sigma_D}{\mathrm{d}Q^2\,\mathrm{d}y\,\mathrm{d}M_X^2} = \frac{N^{\mathrm{rec}} N^{\mathrm{MCgen}} \delta^{\mathrm{rad}} \delta^{p\mathrm{dis}} \delta^{\mathrm{BCC}}}{N^{\mathrm{MCrec}} \mathcal{L} \cdot \mathrm{BV}}\,, \qquad (6)$$

where $N^{\mathrm{rec}}$ is the number of reconstructed data events in the bin after the event selection described in Sect. 4, $N^{\mathrm{MCrec}}$ ($N^{\mathrm{MCgen}}$) is the number of reconstructed (generated) Monte Carlo events in the bin; $\delta^{\mathrm{rad}}$ and $\delta^{\mathrm{BCC}}$ are the radiative correction and bin center correction for inclusive diffraction, respectively. The ratio is then given by:

$$f_D^{c\bar{c}} = \frac{\mathrm{d}^3\sigma_D^{c\bar{c}}}{\mathrm{d}Q^2\,\mathrm{d}y\,\mathrm{d}M_X^2} \Big/ \frac{\mathrm{d}^3\sigma_D}{\mathrm{d}Q^2\,\mathrm{d}y\,\mathrm{d}M_X^2}\,. \qquad (7)$$

### 6.3 Systematic uncertainties

The following sources of systematic uncertainty for the two different analysis methods are taken into account; the estimated values are given in Table 2:

- The simulated trigger efficiencies for the $D^*$ analyses are compared with the efficiencies determined from data using monitor trigger samples. Within the statistics of these data samples the simulated trigger efficiencies are found to agree with the data, with a remaining uncertainty in the range ±(3–5)% depending on the analysis. For the displaced track analysis an uncertainty of 1% is assigned as determined from the data.
- For the DIS measurements the reconstructed polar angle and the energy of the scattered positron are varied within the estimated uncertainties of ±1 mrad for the angular measurement and ±1% for the energy scale of the SpaCal, leading to an uncertainty of ±2% on the cross section measurements. In photoproduction a variation within the estimated uncertainty of ±1.5% on the energy scale of the crystal Čerenkov calorimeter of the electron tagger results in an uncertainty of ±2%.
- The uncertainty of the track reconstruction efficiency and uncertainties related to the signal extraction for the $D^*$ analyses have been determined by analyzing inclusive $D^*$ samples as in [46] and are estimated to be ±6% for the reconstruction efficiency of the three daughter tracks of the $D^*$ meson in the CTD and ±6% for the signal extraction. The uncertainty on the correction for mass reflections is estimated to be ±1.5% [43].
  For the displaced track analysis a track efficiency uncertainty of ±2% due to the CTD and of ±1% due to the CST is estimated, resulting in an uncertainty of ±2% on the cross sections. An uncertainty in the resolution of $\delta$ of the tracks is estimated by varying the resolution by an amount that encompasses the differences between the data and the simulation (see Fig. 3). This is achieved by applying an additional Gaussian smearing in the Monte

**Table 2.** Systematic uncertainties for the measurement of diffractive open charm production for the inclusive cross section in the visible range for the reconstruction of $D^{*\pm}$ mesons in DIS and photoproduction and in the differential bins for the displaced track method in DIS

| Source of uncertainty | Uncertainty (%) | | |
|---|---|---|---|
| | $D^*$ ($\gamma p$) | $D^*$ (DIS) | Displaced track (DIS) |
| Trigger efficiency | 5 | 3 | 1 |
| Scat. $e^+$ energy/angle (1% ⊕ 1 mrad (DIS), 1.5% ($\gamma p$)) | 2 | 2 | 2 |
| Track reconstruction efficiency | 6 | 6 | 2 |
| Signal extraction method ($D^*$) | 6 | 6 | – |
| Reflections ($D^*$) | 1.5 | 1.5 | – |
| $\delta$ resolution (25 $\mu$m ⊕ 200 $\mu$m) | – | – | 2 |
| Hadronic energy scale (4%) | 1 | 1 | 3 |
| QCD model (reweights in $x_{I\!P}$, $\beta$, $Q^2$, $y$) | 1 | 5 | 12–18 |
| Proton diss. model (reweights in $\lvert t\rvert$, $M_Y$, fraction) | 4 | 5 | 5 |
| Noise in FMD and PLUG | 1.5 | 1.5 | 1.5 |
| Tagging efficiency of FMD (10%) | 1 | 1 | 1 |
| Tagging efficiency of PRT ($^{+25}_{-50}$%) | 7 | 9 | 9 |
| Non-diffractive background (100%) | 3 | 1 | 1 |
| reggeon contribution (100%) | 4 | 1 | 1–9 |
| Fragmentation of $c$ quarks | 4 | 1 | 7 |
| Branching fractions/lifetimes/track multiplicities | 2.5 | 2.5 | 3 |
| Asymmetry of $\delta$ for light quarks (±50%) | – | – | 4–16 |
| Beauty fraction ($^{+400}_{-100}$%) | – | – | 0–40 |
| Quark axis ($2^\circ/5^\circ$) | – | – | 3 |
| Luminosity | 1.5 | 1.5 | 1.5 |
| QED correction | – | 2 | 2 |
| Bin center correction | – | – | 8–10 |
| Total | 15 | 15 | 26–47 |

Carlo simulation of $\pm 200\,\mu$m to 5% of randomly selected tracks and $\pm 25\,\mu$m to the rest, resulting in an error of 2% on the cross sections.

- The effect of a $\pm 4\%$ uncertainty in the energy scale of the hadronic final state leads to a change of the cross section in the range $\pm(1$–$3)\%$ depending on the analysis.
- The uncertainty in the acceptance and migration corrections due to uncertainties in the physics models for diffractive charm production is estimated by varying the shape of various kinematic distributions in the Monte Carlo simulation within limits set by the present measurements. Reweighting the shapes of the $x_{I\!P}$, $\beta$ and $Q^2$ distributions by $\left(\frac{1}{x_{I\!P}}\right)^{\pm 0.25}$, $\beta^{\pm 0.3}$ and $(1+\log_{10}(Q^2/\mathrm{GeV}^2))^{\pm 1}$ in DIS results in an uncertainty of $\pm 5\%$ on the total cross section for the $D^*$ analysis and $\pm(12$–$18)\%$ for the displaced track analysis. A variation of the $x_{I\!P}$ and $y$ distributions by $\left(\frac{1}{x_{I\!P}}\right)^{\pm 0.25}$ and $\left(\frac{1}{y}\right)^{\pm 0.2}$ in photoproduction results in an uncertainty of $\pm 1\%$ on the total cross section. The uncertainty on the fraction of the reggeon contribution is estimated by varying its normalization in the simulation by $\pm 100\%$, which leads to an uncertainty of $\pm 1\%$ ($\pm 4\%$) for the $D^*$ analyses in DIS (photoproduction) and $\pm(1$–$9)\%$ for the measurement bins of the displaced track analysis. A variation of the $t$ distribution by $\mathrm{e}^{\pm 2t}$ for proton elastic scattering and the $M_Y$ and the $t$ distribution by $\left(\frac{1}{M_Y^2}\right)^{\pm 0.3}$ and $\mathrm{e}^{\pm 1t}$ for proton dissociative scattering as well as the ratio of proton elastic to proton dissociative scattering between $1:2$ and $2:1$ results in a systematic uncertainty on the cross sections in the range $\pm(4$–$5)\%$.
- The uncertainties for residual noise in the FMD and the PLUG calorimeter in the simulation are estimated using a set of randomly triggered events during the data taking period and result in a combined uncertainty of $\pm 1.5\%$. The tagging efficiency of the PRT for proton dissociative systems with $M_Y > 1.6$ GeV or $|t| > 1\,\mathrm{GeV}^2$ in the simulation is adjusted with the help of an independent non-diffractive data sample with activity in the forward part of the LAr calorimeter and the FMD, where such events are enriched. The effect of the remaining uncertainty on this efficiency on the cross section measurements is estimated by varying the simulation within the statistical accuracy of the measured efficiency and is estimated to lie between $\pm(7$–$9)\%$. The uncertainty on the tagging efficiency of the FMD is estimated to be $\pm 10\%$ [4]. The effect on the cross sections is $\pm 1\%$. The residual influence of non-diffractive background from events without a rapidity gap is estimated by assigning a $\pm 100\%$ uncertainty to the corresponding event samples in the RAPGAP simulation. This leads to an uncertainty on the cross sections in the range $\pm(1$–$3)\%$.
- The uncertainty of the charm fragmentation scheme is estimated by changing the parametrization of the longitudinal fragmentation function from the Lund–Bowler model [35] to Peterson functions with $\epsilon = 0.078$ ($\epsilon = 0.058$) [47] in the simulation of the events for the $D^*$ (displaced track) analyses, which results in an uncertainty on the cross section of $\pm 1\%$ ($\pm 4\%$) for the $D^*$ analyses in DIS (photoproduction) and of $\pm 7\%$ in the displaced track analysis.
- For the displaced track analysis the uncertainties on the lifetimes of the various $D$ mesons, decay branching fractions and mean charge multiplicities are estimated by varying the input values of the Monte Carlo simulation by the errors on the world average measurements. The values and the uncertainties for the lifetimes of the $D$ mesons are taken from [42] and those from the branching fractions of charm quarks to hadrons from [48]. They are consistent with measurements in DIS at HERA [49]. The values and the uncertainties for the mean charged track multiplicities for charm quarks are taken from [50]. A combination of all these uncertainties results in an error of 3% on the cross sections. For the $D^*$ analyses the uncertainty of $\pm 2.5\%$ on the branching fraction for the decay channel in (4) is taken from [42].
- The uncertainty on the asymmetry of the $\delta$ distribution for the light quarks in the displaced track analysis is estimated by repeating the fits with the subtracted light quark significance distributions (shown in Fig. 4) changed by $\pm 50\%$. The light quark asymmetry is checked to be within this uncertainty by comparing the asymmetry of the Monte Carlo events to that of the data, in the region of $0.1 < |\delta| < 0.5$ cm, where the light quark asymmetry is enhanced. This results in an uncertainty on the cross section of $\pm 4\%$ at high $M_X$ and of $\pm 16\%$ at low $M_X$.
  The uncertainty on the beauty contribution for the displaced track analysis is estimated by repeating the fits with the subtracted beauty quark significance distributions (shown in Fig. 4) changed by $^{+400}_{-100}\%$, which results in an negligible error on the cross section at low $M_X$ increasing to $^{-14}_{+5}\%$ and $^{-40}_{+13}\%$ in the middle and high $M_X$ bins, respectively.
- An uncertainty on the quark axis in the displaced track analysis is estimated by shifting it by $\pm 2^\circ$ ($\pm 5^\circ$) for events with (without) a reconstructed jet. These shifts have been estimated in [28] by comparing the difference between $\phi_{\mathrm{quark}}$ and the track azimuthal angle in data and Monte Carlo simulation. The resulting error on the cross sections is $\pm 3\%$.
- The uncertainty in the calculation of QED radiative effects is found to be $\pm 2\%$ in DIS.
- The uncertainty in the bin center correction for the displaced track analysis is estimated by varying the shape of the $Q^2$, $\beta$ and $x_{I\!P}$ distributions of the NLO QCD expectation. This leads to a $\pm(8$–$10)\%$ uncertainty on the cross sections.
- The uncertainty of the luminosity determination is estimated to be $\pm 1.5\%$.

The total systematic uncertainty for each data point has been obtained by adding all individual contributions in quadrature. For the $D^*$ analyses it ranges between 15% and 30% for the differential cross sections and amounts to $\pm 15\%$ for the integrated cross section in both kinematic regimes. For the displaced track analysis it ranges between 26% and 47% for the three points of the inclusive charm cross section measurement.

# 7 QCD calculations

## 7.1 NLO calculations in collinear factorization

The measured charm cross sections are compared with NLO QCD calculations based on two alternative sets of diffractive parton density functions from H1 [4] which both provide a good description of the inclusive diffractive DIS data. As default the standard parameterization H1 2006 DPDF Fit A is chosen. The alternative set of DPDFs (H1 2006 DPDF Fit B) is obtained from a slightly different parameterization of the gluon density at the starting scale of the fit procedure. It leads to a steeper fall-off of the gluon density at higher values of $z_{I\!P}$. In the fit to the inclusive diffractive DIS data [4] charm quarks are treated as massive, appearing via BGF-type processes up to order $\alpha_s^2$ [51, 52]. The quark mass is set to $m_c = 1.4\,\text{GeV}$ and the scale for heavy flavor production to $\mu_r = \mu_f = 2m_c$.

In order to be able to compare the measured $D^*$ cross section to the results based on the NLO QCD fits diffractive versions of the programs HVQDIS [53, 54] in DIS and FMNR [55, 56] in photoproduction are used. The renormalization and the factorization scales are set to $\mu_r = \mu_f = \sqrt{Q^2 + 4m_c^2}$ in DIS and to $\mu_r = \mu_f = \sqrt{p_t^2 + 4m_c^2}$ in photoproduction, respectively. For both calculations the charm mass is chosen to be $m_c = 1.5\,\text{GeV}$. The calculations result in predictions for the production of charm quarks. To obtain predictions for a measurement of $D^*$ meson production hadronization corrections evaluated using the LUND hadronization model as implemented in RAPGAP are applied. For the longitudinal fragmentation Peterson functions are used with $\epsilon = 0.035$ as suggested for NLO predictions by [57]. For the calculation of these corrections parton showers are included to simulate the higher order effects of QCD in the event generation of the LO Monte Carlo program. To estimate the uncertainty of the NLO calculations the renormalization and the factorization scales are simultaneously varied by factors of 1/2 and 2, the charm mass is varied by $\pm 0.2\,\text{GeV}$ and the Peterson fragmentation parameter $\epsilon$ is varied by $\pm 0.025$. The uncertainties originating from all these variations are added in quadrature. They result in a combined uncertainty on the theoretical integrated $D^*$ meson cross section of $\approx 25\%$ in DIS and $\approx 22\%$ in photoproduction.

## 7.2 Two gluon exchange models

The measured $D^*$ cross sections are compared with QCD calculations based on the perturbative two gluon approach of 'BJKLW' [16–20] using the $k_t$ unintegrated gluon density J2003 set2 evolved by the CCFM [58–60] evolution equations obtained from fits [21] to the inclusive DIS cross section. These calculations are applicable only in the region of small $x_{I\!P}$ ($x_{I\!P} < 0.01$), where contributions from secondary reggeon exchanges can be neglected. To ensure that the perturbative calculations are applicable a cut on the transverse momentum of the gluon of $p_t^g > 2.0\,\text{GeV}$ for the process $\gamma^* p \to c\bar{c}gp$ is applied.

## 7.3 The MRW model

The measurements of the diffractive charm cross section in DIS are also compared with the approach of 'MRW' [22–24] which can be considered to be a hybrid of the two approaches described in Sects. 7.1 and 7.2. The parameters of the input DPDFs were determined from a fit to the H1 inclusive diffractive data [22–24]. At low $\beta$, charm is produced via a 'resolved pomeron' mechanism by BGF-type processes calculated up to order $\alpha_s^2$, as in the approach of Sect. 7.1. At high $\beta$, the perturbative two-gluon state participates directly in the hard interaction via 'photon–pomeron' fusion. This 'direct pomeron' contribution is similar to the $\gamma^* p \to c\bar{c}p$ contribution of the BJKLW model and depends on the square of the gluon distribution of the proton.

# 8 Results

In DIS the integrated cross section of diffractive $D^{*\pm}$ production in the kinematic range of $2 < Q^2 < 100\,\text{GeV}^2$, $0.05 < y < 0.7$, $x_{I\!P} < 0.04$, $M_Y < 1.6\,\text{GeV}$, $|t| < 1\,\text{GeV}^2$, $p_t(D^*) > 2\,\text{GeV}$ and $|\eta(D^*)| < 1.5$ is measured to be

$$\sigma(ep \to eD^{*\pm}X'Y)_{\text{DIS}} = 234 \pm 29(\text{stat.}) \pm 34(\text{syst.})\,\text{pb}\,, \tag{8}$$

which is in good agreement with the measurement in the same kinematic range in the previous analysis by H1 [25].

In photoproduction the integrated $ep$ cross section of diffractive $D^{*\pm}$ production in the kinematic range of $Q^2 < 0.01\,\text{GeV}^2$, $0.3 < y < 0.65$, $x_{I\!P} < 0.04$, $M_Y < 1.6\,\text{GeV}$, $|t| < 1\,\text{GeV}^2$, $p_t(D^*) > 2\,\text{GeV}$ and $|\eta(D^*)| < 1.5$ is measured to be

$$\sigma(ep \to eD^{*\pm}X'Y)_{\gamma p} = 265 \pm 50(\text{stat.}) \pm 41(\text{syst.})\,\text{pb}\,. \tag{9}$$

A comparison of the measured integrated cross sections in DIS and photoproduction with the predictions of the NLO calculations for the two sets of H1 2006 DPDFs (Fit A and Fit B) [4] is given in Table 1. A good agreement between the data cross sections and the NLO QCD calculations is observed.

The $D^*$ meson cross section in DIS is also measured differentially as a function of the $D^*$ kinematic variables $p_t(D^*)$ and $\eta(D^*)$, the DIS kinematic variables $y$ and $Q^2$, and the diffractive variables $x_{I\!P}$, $\beta$ and $z_{I\!P}^{\text{obs}}$. They are listed in Table 3 and shown in Figs. 5 and 6. The data are compared in the figures with the predictions of the NLO QCD calculations. For the cross sections as a function of the $D^*$ and DIS kinematic variables the predictions for the two sets of DPDFS are similar with both providing a good description of the data. For the comparison with the diffractive kinematic quantities the differences in the predictions for the two DPDFs are larger, with $z_{I\!P}^{\text{obs}}$ showing the largest sensitivity, where the steeper fall-off of the gluon density in Fit B is reproduced. However, within the present experimental errors

**Table 3.** Differential cross sections for diffractive $D^{*\pm}$ meson production in DIS, as a function of $p_t(D^*)$, $\eta(D^*)$, $y$, $Q^2$, $x_{I\!P}$, $z_{I\!P}^{obs}$ and $\beta$, given in the range of $2 < Q^2 < 100\,\mathrm{GeV}^2$, $0.05 < y < 0.7$, $x_{I\!P} < 0.04$, $M_Y < 1.6\,\mathrm{GeV}$, $|t| < 1\,\mathrm{GeV}^2$, $p_t(D^*) > 2\,\mathrm{GeV}$ and $|\eta(D^*)| < 1.5$

DIS $D^{*\pm}$ meson cross section as a function of $p_t(D^*)$

| Range (GeV) | Bin center (GeV) | $d\sigma/dp_t(D^*)$ (pb/GeV) | $\delta_{stat}$ (%) | $\delta_{syst}$ (%) |
|---|---|---|---|---|
| 2.0–2.5 | 2.20 | 169 | 25 | 16 |
| 2.5–3.0 | 2.75 | 114 | 25 | 15 |
| 3.0–3.6 | 3.35 | 76 | 24 | 15 |
| 3.6–10.0 | 5.45 | 8 | 23 | 15 |

DIS $D^{*\pm}$ meson cross section as a function of $\eta(D^*)$

| Range | Bin center | $d\sigma/d\eta(D^*)$ (pb) | $\delta_{stat}$ (%) | $\delta_{syst}$ (%) |
|---|---|---|---|---|
| −1.5–(−0.75) | −1.17 | 92 | 22 | 15 |
| −0.75–0 | −0.33 | 101 | 21 | 15 |
| 0–0.75 | 0.42 | 81 | 25 | 15 |
| 0.75–1.5 | 1.12 | 40 | 37 | 21 |

DIS $D^{*\pm}$ meson cross section as a function of $y$

| Range | Bin center | $d\sigma/dy$ (pb) | $\delta_{stat}$ (%) | $\delta_{syst}$ (%) |
|---|---|---|---|---|
| 0.05–0.15 | 0.09 | 975 | 18 | 15 |
| 0.15–0.30 | 0.22 | 423 | 25 | 15 |
| 0.30–0.45 | 0.38 | 198 | 37 | 16 |
| 0.45–0.70 | 0.55 | 141 | 37 | 18 |

DIS $D^{*\pm}$ meson cross section as a function of $Q^2$

| Range ($\mathrm{GeV}^2$) | Bin center ($\mathrm{GeV}^2$) | $d\sigma/dQ^2$ (pb/$\mathrm{GeV}^2$) | $\delta_{stat}$ (%) | $\delta_{syst}$ (%) |
|---|---|---|---|---|
| 2.0–5.0 | 4.0 | 17 | 27 | 17 |
| 5.0–15.0 | 9.5 | 7.6 | 21 | 15 |
| 15.0–35.0 | 23.5 | 3.6 | 21 | 14 |
| 35.0–100.0 | 60.5 | 0.6 | 31 | 14 |

DIS $D^{*\pm}$ meson cross section as a function of $\log(x_{I\!P})$

| Range | Bin center | $d\sigma/d\log(x_{I\!P})$ (pb) | $\delta_{stat}$ (%) | $\delta_{syst}$ (%) |
|---|---|---|---|---|
| −3.0–(−2.6) | −2.79 | 36 | 39 | 30 |
| −2.6–(−2.2) | −2.39 | 118 | 22 | 21 |
| −2.2–(−1.8) | −2.01 | 138 | 25 | 15 |
| −1.8–(−1.4) | −1.55 | 275 | 21 | 17 |

DIS $D^{*\pm}$ meson cross section as a function of $z_{I\!P}^{obs}$

| Range | Bin center | $d\sigma/dz_{I\!P}^{obs}$ (pb) | $\delta_{stat}$ (%) | $\delta_{syst}$ (%) |
|---|---|---|---|---|
| 0–0.15 | 0.07 | 312 | 44 | 19 |
| 0.15–0.45 | 0.29 | 325 | 19 | 15 |
| 0.45–1 | 0.69 | 99 | 17 | 30 |

DIS $D^{*\pm}$ meson cross section as a function of $\log(\beta)$

| Range | Bin center | $d\sigma/d\log(\beta)$ (pb) | $\delta_{stat}$ (%) | $\delta_{syst}$ (%) |
|---|---|---|---|---|
| −2.5–(−1.8) | −2.12 | 55 | 40 | 19 |
| −1.8–(−1.2) | −1.57 | 120 | 23 | 14 |
| −1.2–(−0.6) | −0.88 | 123 | 18 | 16 |
| −0.6–0 | −0.28 | 50 | 27 | 21 |

and theoretical uncertainties these differences cannot be resolved. The good description of the NLO QCD calculations for all of the $D^*$, DIS and diffractive kinematic distributions supports the assumption of QCD factorization, in particular, the compatibility of the gluon density obtained from scaling violations in the inclusive diffractive cross section with that required to describe the $D^*$ data.

In photoproduction the $D^*$ cross section is shown differentially as a function of the $D^*$ kinematic variables $p_t(D^*)$ and $\eta(D^*)$ and the kinematic variable $y$ in Fig. 7 and as a function of the diffractive kinematic variables $x_{I\!P}$ and $z_{I\!P}^{obs}$ in Fig. 8. The values are given in Table 4. The data are well described by the theoretical predictions within the larger experimental errors for photoproduction. As in DIS the largest sensitivity to the different parameterizations of the

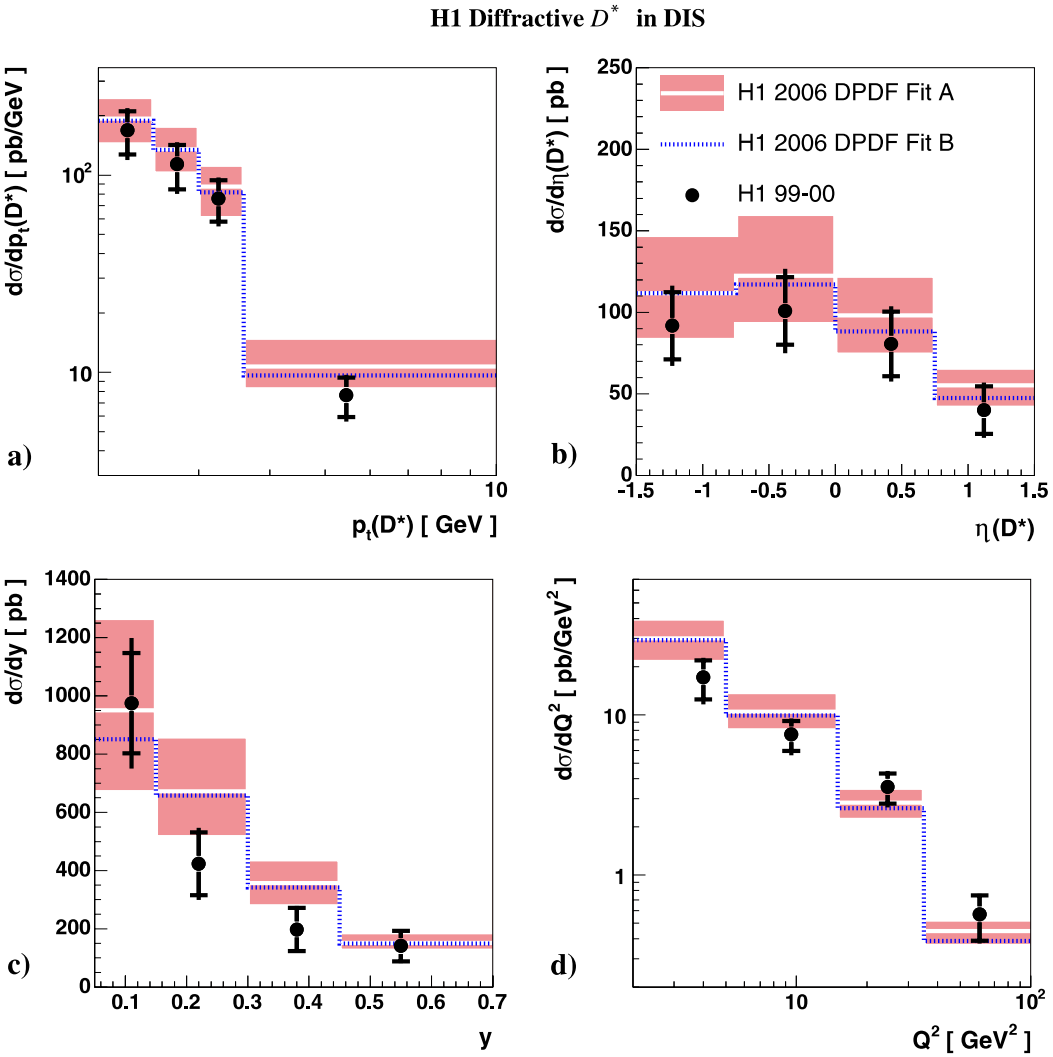


**Fig. 5.** Differential cross sections for diffractive $D^*$ meson production in DIS as a function of **a** $p_t(D^*)$, **b** $\eta(D^*)$, **c** the inelasticity $y$ and **d** the photon virtuality $Q^2$. The *inner error bars* of the *data points* represent the statistical uncertainties of the measurement only, while the *outer error bars* show the statistical and systematic uncertainties added in quadrature. The data are compared with a pQCD calculation in NLO using two alternative sets of diffractive parton density functions (fit A and fit B) extracted by H1 [4]

gluon is evident in the $z_{I\!P}^{\rm obs}$ distribution. The shapes of the $z_{I\!P}^{\rm obs}$ distribution for the predictions in DIS and $\gamma p$ are compatible which is due to the fact that both kinematic regimes probe the diffractive gluon density at a similar scale.

The good agreement of the NLO QCD predictions with the measured cross sections observed in DIS and photoproduction, both in shape and normalization, supports the assumption that QCD factorization is applicable in both kinematic regimes. A quantity, which is less sensitive to the input of diffractive parton density functions and theoretical uncertainties is defined by

$$R_{\rm DIS}^{\gamma p} = \frac{(\sigma^{\rm meas}/\sigma^{\rm theo})_{\gamma p}}{(\sigma^{\rm meas}/\sigma^{\rm theo})_{\rm DIS}}\,, \qquad (10)$$

where $\sigma^{\rm meas}$ and $\sigma^{\rm theo}$ denote the measured and the predicted integrated cross section for $D^*$ production. To reduce theoretical uncertainties due to extrapolations from different regions in $y$ the cross section in DIS is further restricted to the range of $0.3 < y < 0.65$ as for the photoproduction measurement. The DIS cross section in this range is shown in Table 1. The ratio $R_{\rm DIS}^{\gamma p}$ is found to be $1.15 \pm 0.40({\rm stat.}) \pm 0.09({\rm syst.})$, with the systematic uncertainty originating from the model uncertainty on the $\beta$ distribution in DIS, the fragmentation uncertainties and the uncertainties on the reggeon contribution. The theoretical uncertainty on $R_{\rm DIS}^{\gamma p}$ is $\pm 7\%$. The measurement of $R_{\rm DIS}^{\gamma p}$ shows no evidence for a suppression of the photoproduction component although the statistical error of the measurement is large.

In Fig. 9 an additional comparison of both the NLO QCD calculations and of the prediction from the perturbative two gluon calculation of BJKLW [16–20] with differential cross sections in the range of validity of the two gluon model ($x_{I\!P} < 0.01$) are shown. The cross sections are given in Table 5. Within the uncertainties a good agreement between the data and both the NLO QCD calculation and the model of BJLKW is observed. For the two gluon calculation in this kinematic range the $\gamma^* p \to c\bar{c}gp$ contribution is seen to dominate with the $\gamma^* p \to c\bar{c}p$ process contributing only at high values of $z_{I\!P}^{\rm obs}$. Varying the $p_t$ cut-off for the gluon in the $\gamma^* p \to c\bar{c}gp$ process by $\pm 0.5$ GeV leads to a variation of the cross section of $\sim 25\%$ and is also compatible with the data.

The measurements of the diffractive charm DIS cross sections in $Q^2$, $y$ and $M_X^2$ obtained from the displaced

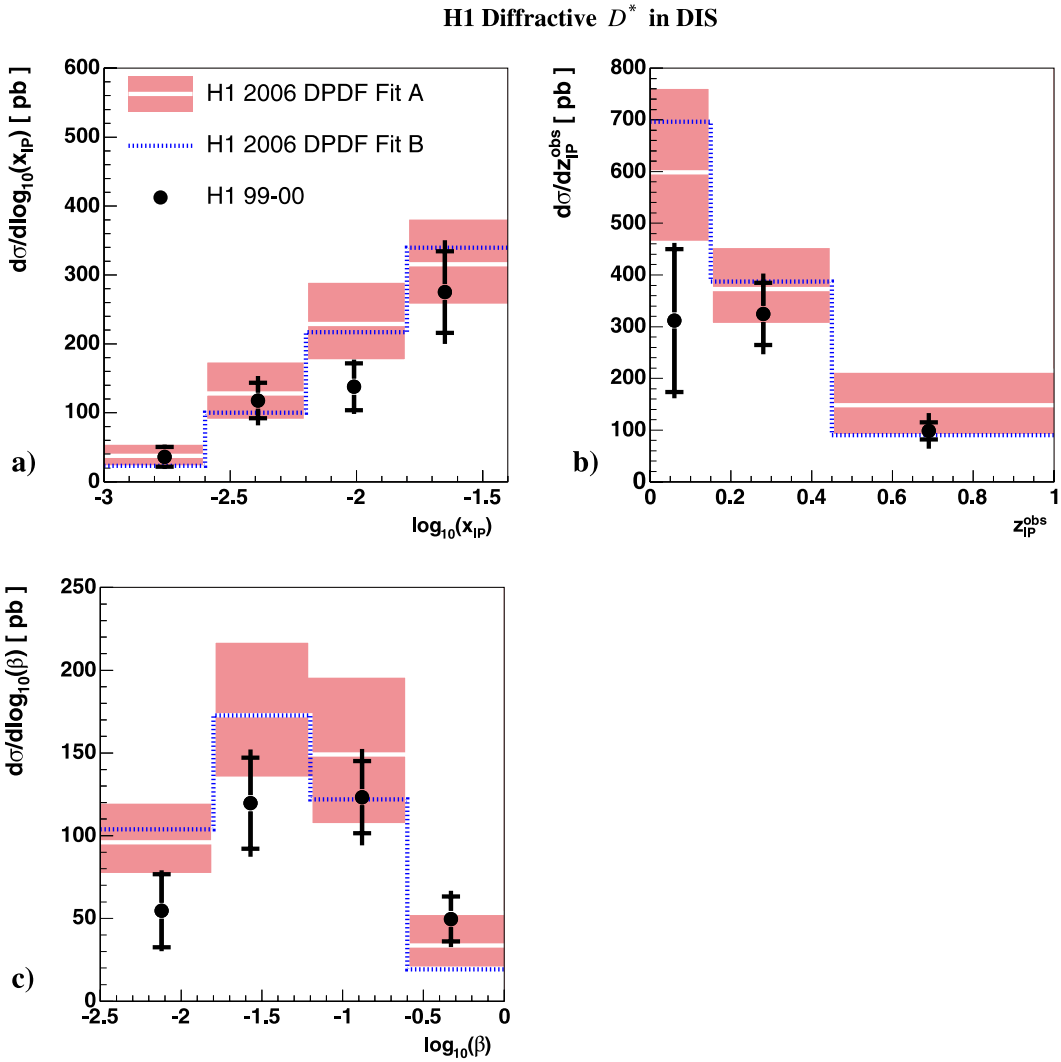


**Fig. 6.** Differential cross sections for diffractive $D^*$ meson production in DIS as a function of **a** $x_{I\!P}$, **b** $z_{I\!P}^{\rm obs}$ and **c** $\beta$. The *inner error bars* of the *data points* represent the statistical uncertainties of the measurement only, while the *outer error bars* show the statistical and systematic uncertainties added in quadrature. The data are compared with a pQCD calculation in NLO using two alternative sets of diffractive parton density functions (fit A and fit B) extracted by H1 [4]

track method are converted to measurements in $x_{I\!P}$, $\beta$ and $Q^2$ using

$$\frac{\mathrm{d}^3\sigma_D^{c\bar{c}}}{\mathrm{d}x_{I\!P}\,\mathrm{d}\beta\,\mathrm{d}Q^2} = \frac{\mathrm{d}^3\sigma_D^{c\bar{c}}}{\mathrm{d}Q^2\,\mathrm{d}y\,\mathrm{d}M_X^2}\frac{sy^2}{\beta}\,. \qquad (11)$$

The diffractive charm reduced cross section is defined as

$$\tilde{\sigma}_D^{c\bar{c}}(x_{I\!P},\beta,Q^2) = \frac{\mathrm{d}^3\sigma_D^{c\bar{c}}}{\mathrm{d}x_{I\!P}\,\mathrm{d}\beta\,\mathrm{d}Q^2}\frac{\beta Q^4}{2\pi\alpha^2(1+(1-y)^2)}\,, \qquad (12)$$

where $\alpha$ is the fine structure constant. The reduced cross section is approximately equal to the charm contribution $F_2^{D(3)c\bar{c}}$ to the diffractive structure function $F_2^{D(3)}$. The difference is due to the contribution from the longitudinal diffractive charm cross section, which is expected to be small for the data points presented in this paper.

The measurements of $x_{I\!P}\tilde{\sigma}_D^{c\bar{c}}$ obtained from the displaced track method are listed in Table 6 and shown in Fig. 10 as a function of $\beta$ for fixed values of $Q^2$ and $x_{I\!P}$. In the figure, the displaced track method data point measured at $x_{I\!P} = 0.01$ is interpolated to $x_{I\!P} = 0.018$ using a parameterization of $\tilde{\sigma}_D^{c\bar{c}}$ from the NLO QCD fit. The measured points of $x_{I\!P}\tilde{\sigma}_D^{c\bar{c}}$ are compared with the results extracted from the $D^*$ meson analysis. For this purpose the $D^*$ cross section is measured in the same $Q^2$, $y$ and $M_X^2$ ranges as for the displaced track method. The results are given in Table 7. These measurements in the visible $D^*$ kinematic range $p_{\rm t}(D^*) > 2$ GeV and $|\eta(D^*)| < 1.5$ are extrapolated with the NLO calculation program HVQDIS to the full $D^*$ kinematic phasespace in order to extract the diffractive open charm cross section. The extrapolation factors are found to be $\approx 2.5$. The NLO calculation program is also used to evaluate the bin center corrections, which are made to the same central values as in the displaced track analysis. The H1 data are also compared with $D^*$ measurements from the ZEUS collaboration [26] which are interpolated to the same kinematic range as the H1 measurement using the NLO QCD fit and corrected with a factor of 1.23 to account for the difference in the measured range from $M_Y = m_p$ to $M_Y < 1.6$ GeV [40]. The measurements for $x_{I\!P}\tilde{\sigma}_D^{c\bar{c}}$ from the displaced track analysis and the $D^*$ extraction methods from both H1 and ZEUS are in good agreement. A comparison with the predictions of the NLO DPDFs shows a good description of the data.

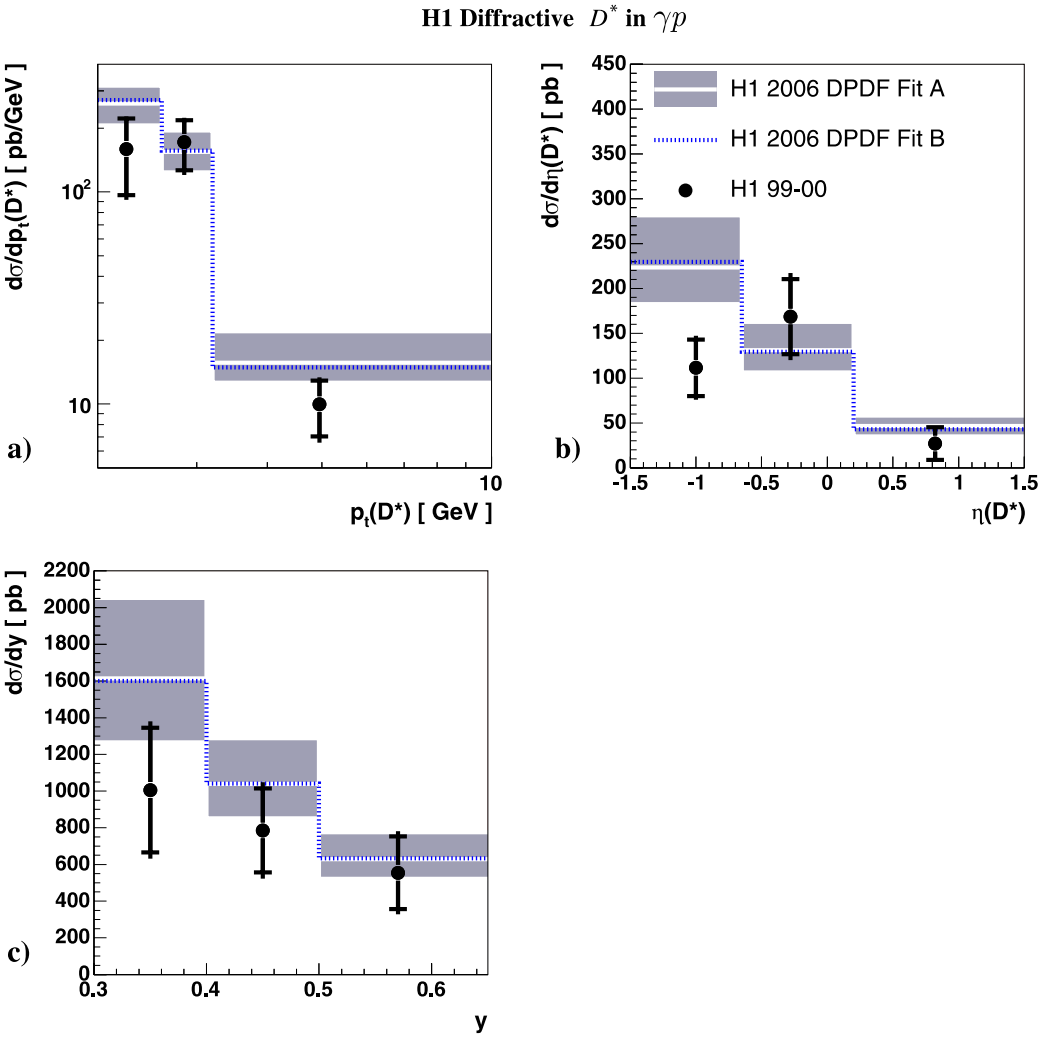


**Fig. 7.** Differential cross sections for diffractive $D^*$ meson production in photoproduction as a function of **a** $p_t(D^*)$, **b** $\eta(D^*)$ and **c** the inelasticity $y$. The *inner error bars* of the *data points* represent the statistical uncertainties of the measurement only, while the *outer error bars* show the statistical and systematic uncertainties added in quadrature. The data are compared with a pQCD calculation in NLO using two alternative sets of diffractive parton density functions (fit A and fit B) extracted by H1 [4]

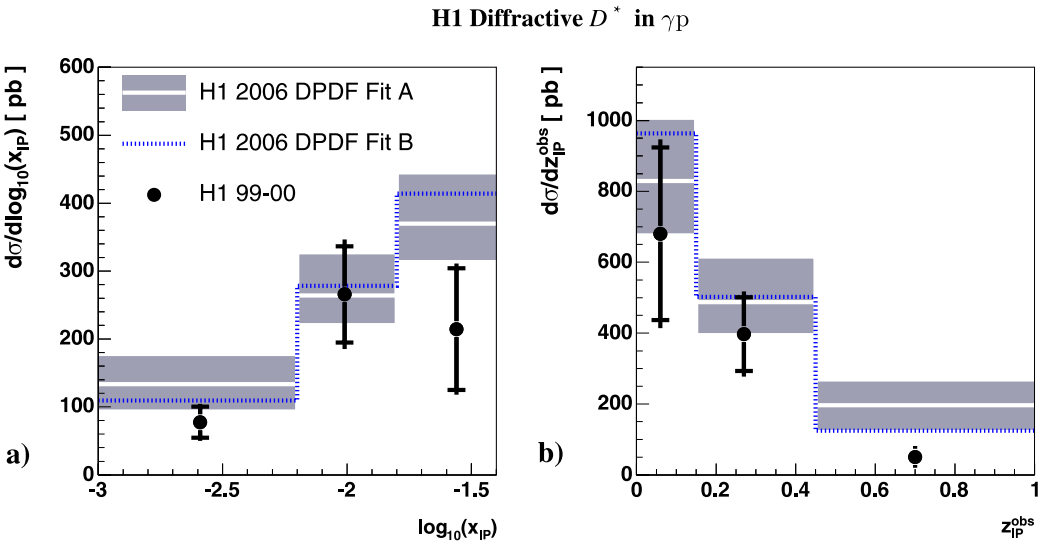


**Fig. 8.** Differential cross sections for diffractive $D^*$ meson production in photoproduction as a function of **a** $x_{I\!P}$ and **b** $z_{I\!P}^{\rm obs}$. The *inner error bars* of the *data points* represent the statistical uncertainties of the measurement only, while the *outer error bars* show the statistical and systematic uncertainties added in quadrature. The data are compared with a pQCD calculation in NLO using two alternative sets of diffractive parton density functions (fit A and fit B) extracted by H1 [4]

In Table 8 and Fig. 11 the measurements are also presented in the form of the fractional contribution of charm to the total diffractive $ep$ cross section $f_D^{c\bar{c}}$. In the given kinematic range the value of $f_D^{c\bar{c}}$ is $\approx 20\%$ on average, which is comparable to the charm fraction in the inclusive cross section at low values of Bjorken $x$ for similar values

**Table 4.** Differential cross sections for diffractive $D^{*\pm}$ meson production in $\gamma p$, as a function of $p_t(D^*)$, $\eta(D^*)$, $y$, $x_{I\!P}$ and $z_{I\!P}^{\rm obs}$, given in the range of $Q^2 < 0.01\,\text{GeV}^2$, $0.3 < y < 0.65$, $x_{I\!P} < 0.04$, $M_Y < 1.6\,\text{GeV}$, $|t| < 1\,\text{GeV}^2$, $p_t(D^*) > 2\,\text{GeV}$ and $|\eta(D^*)| < 1.5$

| $\gamma p$ $D^{*\pm}$ meson cross section as a function of $p_t(D^*)$ | | | | |
|---|---|---|---|---|
| Range (GeV) | Bin center (GeV) | $d\sigma/dp_t(D^*)$ (pb/GeV) | $\delta_{\rm stat}$ (%) | $\delta_{\rm syst}$ (%) |
| 2.0–2.6 | 2.25 | 160 | 39 | 16 |
| 2.6–3.2 | 2.95 | 172 | 26 | 14 |
| 3.2–10.0 | 4.95 | 10 | 29 | 17 |
| $\gamma p$ $D^{*\pm}$ meson cross section as a function of $\eta(D^*)$ | | | | |
| Range | Bin center | $d\sigma/d\eta(D^*)$ (pb) | $\delta_{\rm stat}$ (%) | $\delta_{\rm syst}$ (%) |
| −1.5–(−0.65) | −1.05 | 112 | 28 | 15 |
| −0.65–0.20 | −0.28 | 169 | 25 | 15 |
| 0.20–1.50 | 0.82 | 27 | 67 | 23 |
| $\gamma p$ $D^{*\pm}$ meson cross section as a function of $y$ | | | | |
| Range | Bin center | $d\sigma/dy$ (pb) | $\delta_{\rm stat}$ (%) | $\delta_{\rm syst}$ (%) |
| 0.30–0.40 | 0.35 | 1010 | 34 | 16 |
| 0.40–0.50 | 0.45 | 785 | 29 | 16 |
| 0.50–0.65 | 0.57 | 555 | 36 | 20 |
| $\gamma p$ $D^{*\pm}$ meson cross section as a function of $\log(x_{I\!P})$ | | | | |
| Range | Bin center | $d\sigma/d\log(x_{I\!P})$ (pb) | $\delta_{\rm stat}$ (%) | $\delta_{\rm syst}$ (%) |
| −3.0–(−2.2) | −2.59 | 77 | 30 | 19 |
| −2.2–(−1.8) | −2.01 | 266 | 27 | 15 |
| −1.8–(−1.4) | −1.61 | 214 | 42 | 17 |
| $\gamma p$ $D^{*\pm}$ meson cross section as a function of $z_{I\!P}^{\rm obs}$ | | | | |
| Range | Bin center | $d\sigma/dz_{I\!P}^{\rm obs}$ (pb) | $\delta_{\rm stat}$ (%) | $\delta_{\rm syst}$ (%) |
| 0–0.15 | 0.06 | 680 | 36 | 16 |
| 0.15–0.45 | 0.28 | 400 | 26 | 15 |
| 0.45–1 | 0.70 | 51 | 37 | 48 |

**Table 5.** Differential cross sections for diffractive $D^{*\pm}$ meson production in DIS, in the same kinematic region as that given in Table 3 but further restricted to $x_{I\!P} < 0.01$

| DIS $D^{*\pm}$ meson cross section as a function of $p_t(D^*)$ | | | | |
|---|---|---|---|---|
| Range (GeV) | Bin center (GeV) | $d\sigma/dp_t(D^*)$ (pb/GeV) | $\delta_{\rm stat}$ (%) | $\delta_{\rm syst}$ (%) |
| 2.0–3.0 | 2.45 | 58 | 23 | 18 |
| 3.0–10.0 | 4.95 | 5 | 22 | 18 |
| DIS $D^{*\pm}$ meson cross section as a function of $\eta(D^*)$ | | | | |
| Range | Bin center | $d\sigma/d\eta(D^*)$ (pb) | $\delta_{\rm stat}$ (%) | $\delta_{\rm syst}$ (%) |
| −1.5–0 | −0.65 | 48 | 18 | 17 |
| 0–1.5 | −0.33 | 16 | 34 | 23 |
| DIS $D^{*\pm}$ meson cross section as a function of $\log(x_{I\!P})$ | | | | |
| Range | Bin center | $d\sigma/d\log(x_{I\!P})$ (pb) | $\delta_{\rm stat}$ (%) | $\delta_{\rm syst}$ (%) |
| −3.0–(−2.5) | −2.71 | 43 | 32 | 30 |
| −2.5–(−2.0) | −2.25 | 143 | 19 | 17 |
| DIS $D^{*\pm}$ meson cross section as a function of $z_{I\!P}^{\rm obs}$ | | | | |
| Range | Bin center | $d\sigma/dz_{I\!P}^{\rm obs}$ (pb) | $\delta_{\rm stat}$ (%) | $\delta_{\rm syst}$ (%) |
| 0–0.5 | 0.27 | 74 | 31 | 16 |
| 0.5–1 | 0.69 | 91 | 19 | 42 |

of $Q^2$ [28]. The NLO QCD predictions shown in Fig. 11 are found to describe the data well.

In Figs. 12 and 13 the $x_{I\!P}\tilde{\sigma}_D^{c\bar{c}}$ and $f_D^{c\bar{c}}$ data are compared with the predictions of the MRW model [22–24]. In the kinematic range of the measurements the 'resolved pomeron' contribution, where charm is generated via BGF, is seen to dominate in the model at low $\beta$, while the 'direct pomeron' process, where charm is generated via 'photon–

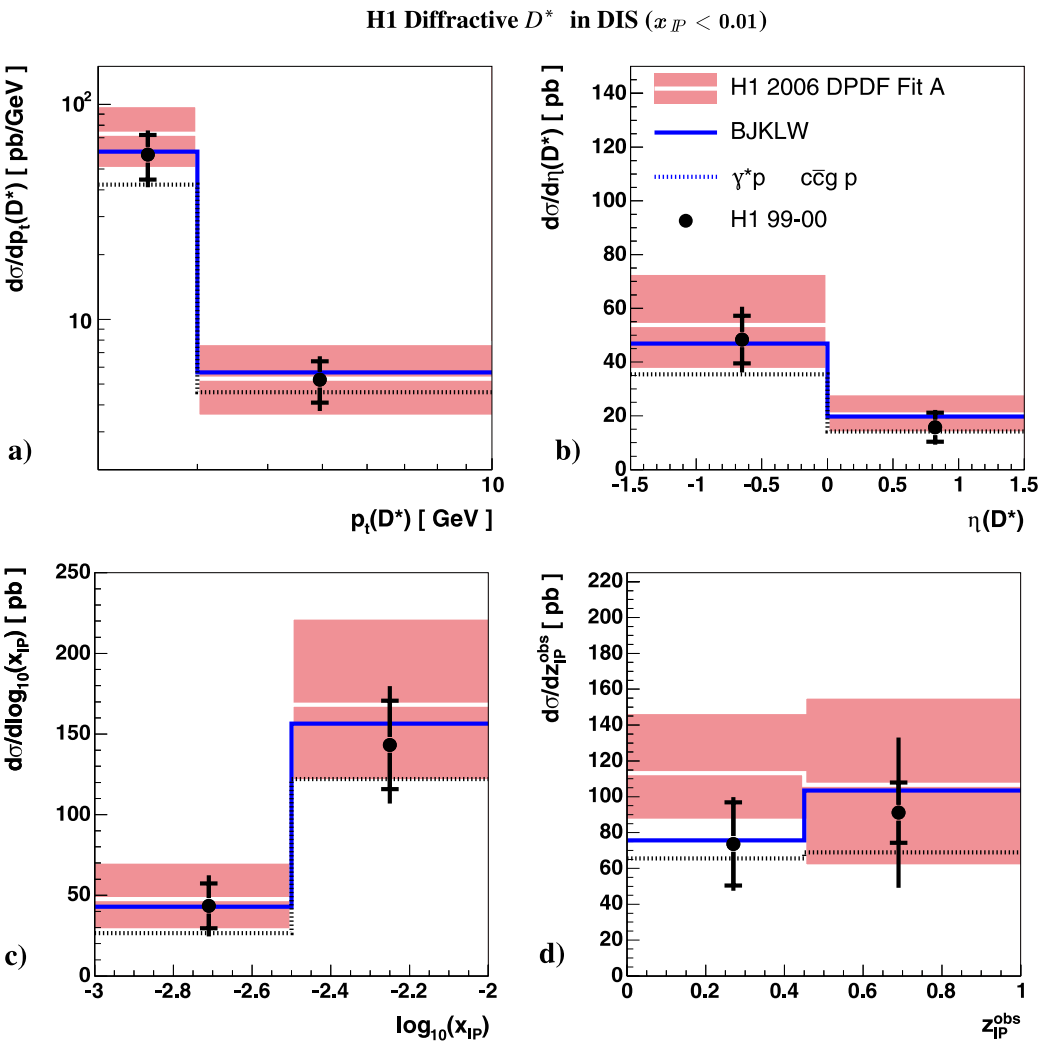


**Fig. 9.** Differential cross sections for diffractive $D^*$ meson production in DIS, in the restricted kinematic region of $x_{I\!P} < 0.01$, shown as a function of **a** $p_t(D^*)$, **b** $\eta(D^*)$, **c** $x_{I\!P}$ and **d** $z_{I\!P}^{obs}$. The *inner error bars* of the *data points* represent the statistical uncertainties of the measurement only, while the *outer error bars* show the statistical and systematic uncertainties added in quadrature. The data are compared with a pQCD calculation in NLO and to a prediction from the perturbative two gluon approach of BJKLW [16–20] with a cut for the gluon momentum in the $\gamma^*p \to c\bar{c}gp$ process of $p_t > 2.0$ GeV. The *dashed line* indicates the resolved $\gamma^*p \to c\bar{c}gp$ contribution only while the *solid line* shows the sum of the $\gamma^*p \to c\bar{c}gp$ and the $\gamma^*p \to c\bar{c}p$ contributions

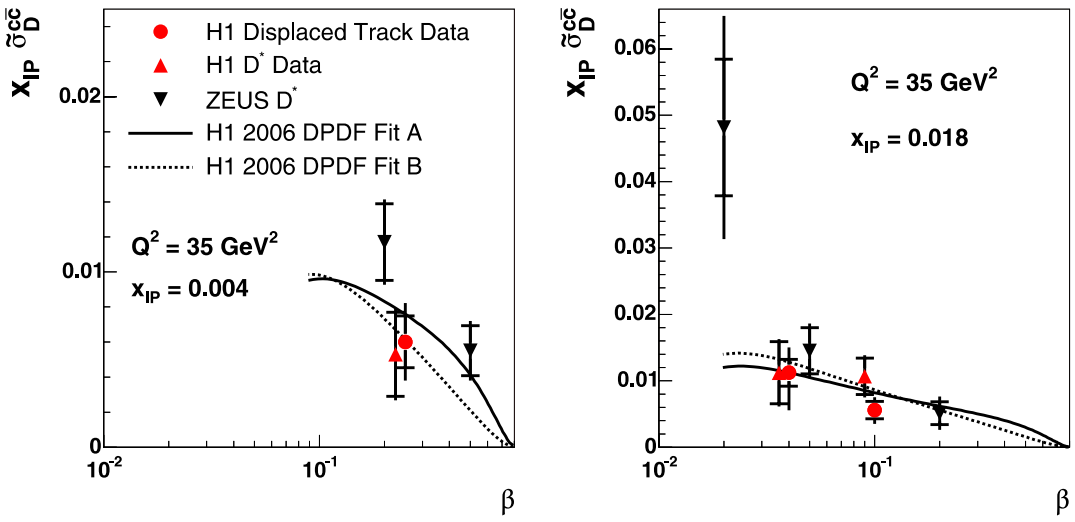


**Fig. 10.** The measured reduced cross section $x_{I\!P}\tilde{\sigma}_D^{c\bar{c}}$ shown as a function of $\beta$ for two different values of $x_{I\!P}$. The *inner error bars* of the *data points* represent the statistical error, while the *outer error bars* represent the statistical and systematic uncertainties added in quadrature. The measurements obtained from $D^*$ mesons from H1 in this paper and from ZEUS [26] are also shown. Measurements at the same values of $\beta$ are displaced for visibility. The measurements are compared with NLO predictions based on two alternative sets of diffractive parton density functions (fit A and fit B) extracted by H1 [4]

**Table 6.** The reduced cross section $\tilde{\sigma}_D^{c\bar{c}}(x_{I\!P}, \beta, Q^2)$ obtained from the displaced track method. The last column shows the results obtained by extrapolating the $D^*$ cross sections in Table 7 using the H1 NLO QCD fit

| Reduced cross section $\tilde{\sigma}_D^{c\bar{c}}(x_{I\!P}, \beta, Q^2)$ | | | | | | |
|---|---|---|---|---|---|---|
| Displaced track | | | | | | $D^*$ |
| $Q^2$ (GeV$^2$) | $x_{I\!P}$ | $\beta$ | $\tilde{\sigma}_D^{c\bar{c}}$ | $\delta_{\rm stat}$ (%) | $\delta_{\rm sys}$ (%) | $\tilde{\sigma}_D^{c\bar{c}}$ |
| 35 | 0.004 | 0.25 | 1.50 | 25 | $^{+27}_{-27}$ | 1.33 |
| 35 | 0.010 | 0.10 | 0.63 | 23 | $^{+26}_{-29}$ | 1.20 |
| 35 | 0.018 | 0.04 | 0.62 | 18 | $^{+29}_{-47}$ | 0.62 |

**Table 7.** The differential cross section for diffractive $D^*$ production in DIS as a function of $M_X$ measured in the range $15 < Q^2 < 100$ GeV$^2$, $0.07 < y < 0.7$, $x_{I\!P} < 0.04$, $M_Y < 1.6$ GeV, $|t| < 1$ GeV$^2$, $p_{\rm t}(D^*) > 2.0$ GeV and $|\eta(D^*)| < 1.5$

| DIS $D^{*\pm}$ meson cross section as a function of $M_X$ | | | |
|---|---|---|---|
| Range (GeV) | $\mathrm{d}\sigma/\mathrm{d}M_X$ (pb/GeV) | $\delta_{\rm stat}$ (%) | $\delta_{\rm sys}$ (%) |
| 6–12 | 2.5 | 45 | 20 |
| 12–20 | 5.0 | 26 | 15 |
| 20–99 | 0.39 | 42 | 17 |

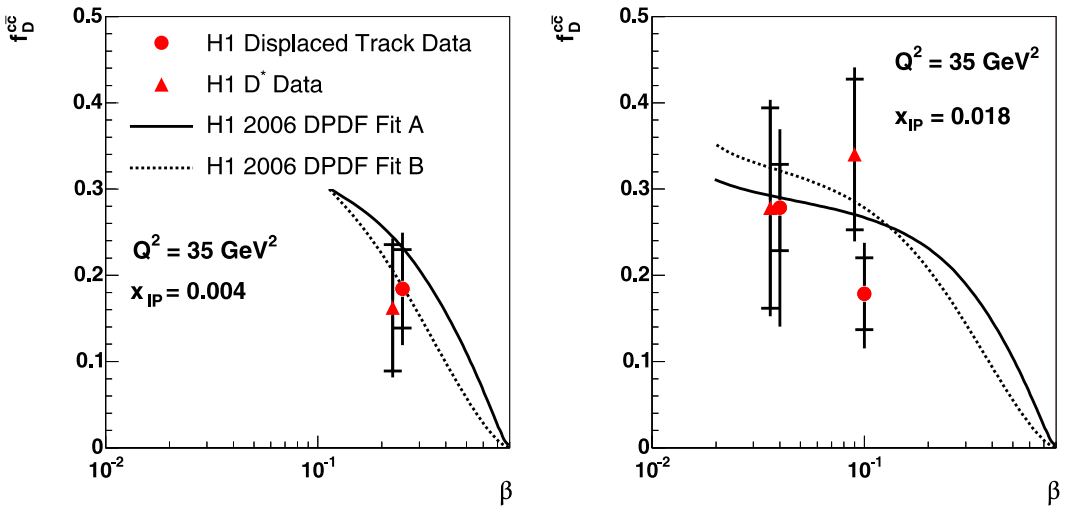


**Fig. 11.** The contribution of charm quarks to the total diffractive cross section $f_D^{c\bar{c}}$ shown as a function of $\beta$ for two different values of $x_{I\!P}$. The *inner error bars* of the *data points* represent the statistical uncertainties, while the *outer error bars* represent the statistical and systematic uncertainties added in quadrature. The measurements are compared with NLO predictions based on two alternative sets of diffractive parton density functions (fit A and fit B) extracted by H1 [4]

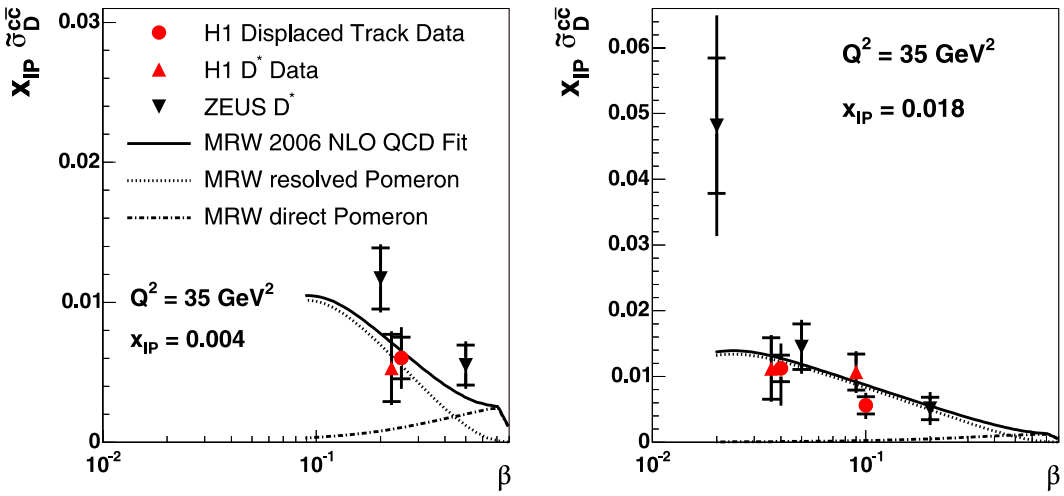


**Fig. 12.** The measured reduced cross section $x_{I\!P}\tilde{\sigma}_D^{c\bar{c}}$ shown as a function of $\beta$ for two different values of $x_{I\!P}$. The *inner error bars* of the *data points* represent the statistical error, while the *outer error bars* represent the statistical and systematic uncertainties added in quadrature. The measurements obtained from $D^*$ mesons from H1 in this paper and from ZEUS [26] are also shown. The measurements are compared with the model of MRW [22–24] based on perturbative two gluon exchange and DPDFs

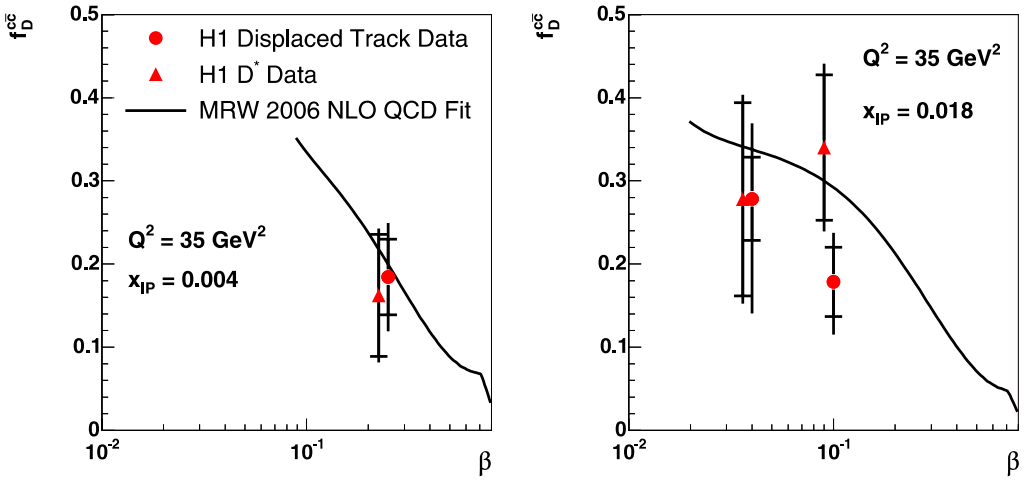


**Fig. 13.** The contribution of charm quarks to the total diffractive cross section $f_D^{c\bar{c}}$ shown as a function of $\beta$ for two different values of $x_{I\!P}$. The *inner error bars* of the *data points* represent the statistical uncertainties, while the *outer error bars* represent the statistical and systematic uncertainties added in quadrature. The measurements are compared with the model of MRW [22–24] based on perturbative two gluon exchange and DPDFs

**Table 8.** The fractional charm contribution to the diffractive cross section $f_D^{c\bar{c}}$ obtained from the displaced track method. The last column shows the results obtained by extrapolating the $D^*$ cross sections in Table 7 using the H1 NLO QCD fit and dividing by the measured total diffractive cross section

| | | Fractional charm contribution $f_D^{c\bar{c}}$ | | | | |
|---|---|---|---|---|---|---|
| | | Displaced track | | | | $D^*$ |
| $Q^2$ (GeV$^2$) | $x_{I\!P}$ | $\beta$ | $f_D^{c\bar{c}}$ | $\delta_{\rm stat}$ (%) | $\delta_{\rm syst}$ (%) | $f_D^{c\bar{c}}$ |
| 35 | 0.004 | 0.25 | 0.184 | 25 | $^{+25}_{-25}$ | 0.162 |
| 35 | 0.010 | 0.10 | 0.193 | 23 | $^{+23}_{-27}$ | 0.367 |
| 35 | 0.018 | 0.04 | 0.278 | 18 | $^{+27}_{-46}$ | 0.278 |

pomeron' fusion is significant at high values of $\beta$. A good description of the data is observed supporting the validity of the DPDFs extracted in this model.

## 9 Conclusions

Measurements are presented of the diffractive charm cross section using two independent methods of charm reconstruction. In the first method charm quarks are tagged using $D^*$ mesons. In the second method tracks, with a significant displacement from the primary vertex, are reconstructed using the CST of H1. These displaced tracks arise due to the long lifetime of charmed hadrons.

The diffractive $D^*$ cross section is measured in DIS and photoproduction. The integrated cross section in DIS is in good agreement with a former measurement of H1, which was obtained from an independent dataset with less than half the luminosity of the present measurement. This is the first cross section measurement of diffractive open charm photoproduction at HERA. A comparison with QCD calculations in NLO based on DPDFs obtained from inclusive diffractive scattering at H1 is in good agreement with the measurement in both kinematic regimes. No evidence is observed for a suppression in photoproduction. In the region of $x_{I\!P} < 0.01$ the DIS $D^*$ data are found to be also well described by a model based on perturbative two gluon exchange and $k_{\rm t}$-factorization.

The displaced track measurements are made at $Q^2 = 35\,{\rm GeV}^2$ for 3 different values of $x_{I\!P}$ and $\beta$. In this kinematic range the charm contribution to the inclusive diffractive cross section is found to be $\approx 20\%$ on average which is compatible with the charm fraction in inclusive DIS found at low values of Bjorken $x$ for similar values of $Q^2$. The cross sections are found to be in good agreement with the measurements extrapolated from the $D^*$ cross section results and to be well described by the predictions of NLO QCD. At low $x_{I\!P}$, the data are found to be also well described by a hybrid model based on two gluon exchange and diffractive parton densities.

*Acknowledgements.* We are grateful to the HERA machine group whose outstanding efforts have made this experiment possible. We thank the engineers and technicians for their work in constructing and maintaining the H1 detector, our funding agencies for financial support, the DESY technical staff for continual assistance and the DESY directorate for support and for the hospitality which they extend to the non DESY members of the collaboration.

## References

1. J.C. Collins, Phys. Rev. D **57**, 3051 (1998) [hep-ph/9709499]
2. J.C. Collins, Phys. Rev. D **61**, 019 902 (2000) [Erratum]
3. H1 Collaboration, C. Adloff et al., Z. Phys. C **76**, 613 (1997)

4. H1 Collaboration, A. Aktas et al., Eur. Phys. J. C **48**, 715 (2006)
5. G. Ingelman, P. Schlein, Phys. Lett. B **152**, 256 (1985)
6. A. Donnachie P. Landshoff, Phys. Lett. B **191**, 309 (1987)
7. A. Donnachie P. Landshoff, Phys. Lett. B **198**, 590 (1987) [Erratum]
8. V. Gribov, L. Lipatov, Sov. J. Nucl. Phys. **15**, 438 (1972)
9. V. Gribov, L. Lipatov, Sov. J. Nucl. Phys. **15**, 675 (1972)
10. Y. Dokshitzer, Sov. Phys. JETP **45**, 641 (1977)
11. G. Altarelli, G. Parisi, Nucl. Phys. B **126**, 298 (1977)
12. H1 Collaboration, C. Adloff et al., Eur. Phys. J. C **6**, 421 (1999) [hep-ex/9808013]
13. H1 Collaboration, C. Adloff et al., Eur. Phys. J. C **20**, 29 (2001) [hep-ex/0012051]
14. S. Schätzel, PhD thesis, (Univ. Heidelberg, 2004), available from http://www-h1.desy.de/publications/theses_list.html
15. CDF Collaboration, T. Affolder et al., Phys. Rev. Lett. **84**, 5043 (2000)
16. J. Bartels, H. Lotter, M. Wüsthoff, Phys. Lett. B **379**, 239 (1996) [hep-ph/9602363]
17. J. Bartels, H. Lotter, M. Wüsthoff, Phys. Lett. B **382**, 449 (1996) [Erratum]
18. J. Bartels, C. Ewerz, H. Lotter, M. Wüsthoff, Phys. Lett. B **386**, 389 (1996) [hep-ph/9605356]
19. J. Bartels, H. Jung, M. Wüsthoff, Eur. Phys. J. C **11**, 111 (1999) [hep-ph/9903265]
20. J. Bartels, H. Jung, A. Kyrieleis, Eur. Phys. J. C **24**, 555 (2002) [hep-ph/0204269]
21. M. Hansson, H. Jung, in: Proc. 11th International Workshop on Deep Inelastic Scattering (DIS 2003), St. Petersburg, Russia, April 2003, ed. by V.T. Kim, L.N. Lipatov, p. 488 [hep-ph/0309009]
22. A.D. Martin, M.G. Ryskin, G. Watt, Eur. Phys. J. C **44**, 69 (2005) [hep-ph/0504132]
23. G. Watt, Proc. Workshop on New Trends in HERA Physics, Ringberg Castle, Germany, 2005, ed. by G. Grindhammer et al., p. 303 [hep-ph/0511333]
24. A.D. Martin, M.G. Ryskin, G. Watt, hep-ph/0609273
25. H1 Collaboration, C. Adloff et al., Phys. Lett. B **520**, 191 (2001) [hep-ex/0108047]
26. ZEUS Collaboration, S. Chekanov et al., Nucl. Phys. B **672**, 3 (2003) [hep-ex/0307068]
27. H1 Collaboration, A. Aktas et al., Eur. Phys. J. C **40**, 349 (2005) [hep-ex/0411046]
28. H1 Collaboration, A. Aktas et al., Eur. Phys. J. C **45**, 23 (2006) [hep-ex/0507081]
29. H1 Collaboration, I. Abt et al., Nucl. Instrum. Methods A **386**, 310 (1997)
30. H1 Collaboration, I. Abt et al., Nucl. Instrum. Methods A **386**, 348 (1997)
31. D. Pitzl et al., Nucl. Instrum. Methods A **454**, 334 (2000) [hep-ex/0002044]
32. H1 Collaboration, R.D. Apphuhn et al., Nucl. Instrum. Methods A **386**, 397 (1997)
33. R. Brun et al., GEANT 3 User's Guide, 1987, CERN-DD/EE/84-1
34. H. Jung, Comput. Phys. Commun. **86**, 147 (1995), see also http://www-h1.desy.de/~jung/rapgap.html
35. B. Andersson, G. Gustafson, G. Ingelman, T. Sjöstrand, Phys. Rep. **97**, 31 (1983)
36. A. Kwiatkowski, H. Spiesberger, H.J. Möhring, Comput. Phys. Commun. **69**, 155 (1992)
37. M. Glück, E. Reya, A. Vogt, Phys. Rev. D **45**, 3986 (1992)
38. M. Glück, E. Reya, A. Vogt, Phys. Rev. D **46**, 1973 (1992)
39. B. List, Diploma thesis (Techn. Univ. Berlin, 1993), available from http://www-h1.desy.de/publications/theses_list.html
40. H1 Collaboration, A. Aktas et al., Eur. Phys. J. C **48**, 749 (2006)
41. T. Sjöstrand, Comput. Phys. Commun. **135**, 238 (2001) [hep-ph/0010017]
42. S. Eidelman et al., Phys. Lett. B **592**, 1 (2004)
43. S. Hengstmann, PhD thesis (Univ. Zürich, 2000), available from http://www-h1.desy.de/publications/theses_list.html
44. S.D. Ellis, D.E. Soper, Phys. Rev. D **48**, 3160 (1993) [hep-ph/9305266]
45. S. Catani, Y.L. Dokshitzer, M.H. Seymour, B.R. Webber, Nucl. Phys. B **406**, 187 (1993)
46. H1 Collaboration, submitted to Eur. Phys. J. C [hep-ex/0608042]
47. C. Peterson, D. Schlatter, I. Schmitt, P.M. Zerwas, Phys. Rev. D **27**, 105 (1983)
48. L. Gladilin, hep-ex/9912064
49. H1 Collaboration, A. Aktas et al., Eur. Phys. J. C **38**, 447 (2005) [hep-ex/0408149]
50. MARK III Collaboration, D. Coffman et al., Phys. Lett. B **263**, 135 (1991)
51. E. Laenen, S. Riemersma, J. Smith, W.L. van Neerven, Nucl. Phys. B **392**, 162 (1993)
52. E. Laenen, S. Riemersma, J. Smith, W.L. van Neerven, Nucl. Phys. B **392**, 229 (1993)
53. B.W. Harris, J. Smith, Nucl. Phys. B **452**, 109 (1995) [hep-ph/9503484]
54. L. Alvero, J.C. Collins, J.J. Whitmore, PSU-TH- **200**, 13 (1998) [hep-ph/9806340]
55. S. Frixione, M.L. Mangano, P. Nason, G. Ridolfi, Phys. Lett. B **348**, 633 (1995) [hep-ph/9412348]
56. S. Frixione, P. Nason, G. Ridolfi, Nucl. Phys. B **454**, 3 (1995) [hep-ph/9506226]
57. P. Nason, C. Oleari, Nucl. Phys. B **565**, 245 (2000)
58. M. Ciafaloni, Nucl. Phys. B **296**, 49 (1988)
59. S. Catani, F. Fiorani, G. Marchesini, Phys. Lett. B **234**, 339 (1990)
60. S. Catani, F. Fiorani, G. Marchesini, Nucl. Phys. B **336**, 18 (1990)